This is a preprint, the final version is subject to change, of the American Mineralogist (MSA)
Cite as Authors (Year) Title. American Mineralogist, in press.
DOI: https://doi.org/10.2138/am-2019-6848

Phase, morphology, elemental composition and formation mechanisms of biogenic and abiogenic Fe-Cu-sulfide nanoparticles: A comparative study on their occurrences under anoxic conditions

Muammar Mansor[1*], Debora Berti[2,3], Michael F. Hochella, Jr.[2,4], Mitsuhiro Murayama[2,4], Jie Xu[1*]

[1]Department of Geological Sciences, the University of Texas at El Paso, El Paso, TX 79968, USA.

[2]Virginia Tech National Center for Earth and Environmental Nanotechnology (NanoEarth), Blacksburg, VA 24061, USA.

[3]Present address: Oceanography Department, Texas A&M University, College Station, TX 77845-3146, USA.

[4]Energy and Environment Directorate, Pacific Northwest National Laboratory, Richland, WA 99354, USA.

[5]Department of Material Science and Engineering, Virginia Tech, Blacksburg, VA 24061, USA

*Corresponding authors: mbmansor@utep.edu or jxu2@utep.edu

Abstract

We report on a systematic study on the physicochemical attributes of synthetic Fe-Cu-sulfide nanoparticles (NPs) precipitated under conditions similar to the anoxic, low temperature aqueous, sedimentary, soil and subsurface environments where these NPs have been repeatedly identified. Characterizing the basic attributes of these NPs is the first step in understanding their

behaviors in various processes including in the bio-availability of essential and toxic metals, environmental remediation and resource recovery. All experiments are performed in the presence and absence of the sulfate-reducer *Desulfovibrio vulgaris* to elucidate biological controls on NP formation. First, the single-metal endmember NPs are determined by precipitation in solution containing either aqueous Fe(II) or Cu(II). Limited differences are observed between biogenic and abiogenic precipitates aged for up to one month; the Fe-only experiments resulted in 4-10 nm mackinawite (FeS) NPs that aggregate to form nanosheets up to ~1,000 nm in size, while the Cu-only experiments resulted in mixtures of covellite (CuS) NPs comprised of <10 nm fine nanocrystals, 20-40 x 6-9 nm nanorods and ~30 nm nanoplates. The crystal sizes of biogenic mackinawite and covellite are respectively larger and smaller than their abiogenic counterparts, indicating a mineral-specific response to biological presence. Structural defects are observable in the fine nanocrystals and nanorods of covellite in both biogenic and abiogenic experiments, indicative of intrinsic NP instability and formation mechanism via particle attachment. In contrast, covellite nanoplates are defect-free, indicating high stability and potentially rapid recrystallization following particle attachment. Next, mixed-metal sulfide NPs are precipitated at variable initial aqueous Fe-to-Cu ratios (2:1, 1:1 and 1:5). With increasing ratio of Fe-to-Cu, Fe-rich covellite, nukundamite ($Cu_{5.5}FeS_{6.5}$), chalcopyrite ($CuFeS_2$), and Cu-rich mackinawite are formed. The Fe-rich covellite NPs are larger (100-200 nm) than covellite precipitated in the absence of Fe, indicating a role for Fe in promoting crystal growth. Chalcopyrite and nukundamite are formed through incorporation of Fe into precursor covellite NPs while retaining the original crystal morphology, as confirmed by doping a covellite suspension with aqueous Fe(II), resulting in the formation of chalcopyrite and nukundamite within days. Additionally, in the biological systems we observe the recrystallization of mackinawite to greigite (Fe_3S_4) after

six months of incubation in the absence of Cu, and the selective formation of chalcopyrite and nukundamite at lower initial Fe-to-Cu ratios compared to abiotic systems. These observations are consistent with NP precipitation that are influenced by the distinct (sub)micro-environments around bacterial cells compared to the bulk solution. Comparative TEM analyses indicate that the synthetic NPs are morphologically similar to NPs identified in natural environments, opening ways to studying behaviors of natural NPs using experimental approaches.

Keywords: metal sulfide nanoparticle, mackinawite, covellite, chalcopyrite, greigite, biomineral

Introduction

Metal sulfide nanoparticles (NPs) such as FeS, CuS and ZnS, are being increasingly recognized as important and understudied components in the biogeochemical cycling of sulfur and heavy metals in a variety of natural settings (e.g. Luther and Rickard, 2005; Hochella et al., 2008; Sharma et al., 2015). In environments such as floodplain soils and estuaries, the precipitation and dissolution of metal sulfide NPs under variable redox conditions affect the sequestration and release of toxic metals into the ecosystem and surrounding waters (Weber et al., 2009a; Fulda et al., 2013; Hofacker et al., 2013; Niu et al., 2018). In heavy-metal contaminated riverbeds and subsurface aquifer sediments, the phase and morphology of metal sulfide NPs formed *in situ* greatly affect the efficiency of environmental remediation via heavy metal immobilization (Labrenz et al. 2000; Moreau et al. 2004; Hochella et al. 2005; Qafoku et al. 2014; Xu et al. 2017). The formation of metal sulfide NPs also act as an important step for resource recovery of precious metals from mine tailings and industrial processes (Liang et al.

2012; Falagán et al. 2017). Additionally, metal sulfide NPs released from hydrothermal vents on seafloors are important carriers of trace metal nutrients to the ocean (Yücel et al. 2011; Gartman et al. 2014). The ubiquity of metal sulfide NPs, their higher stabilities compared to aqueous phases, and their unique properties such as high surface reactivity compared to their larger counterparts lend them an important role in mediating the biogeochemical cycling of elements and in maintaining the balance of microbial ecology.

The high reactivity of metal sulfide NPs stems from a number of properties unique at the nano-scale that disappears once minerals reach sizes greater than several to many tens of nanometers. Nanoparticles are characterized by high surface areas and high concentration of atomic defects near the crystal surface that provide active reaction sites (e.g. Banfield and Zhang, 2001; Hochella et al., 2008; Eskelsen et al., 2018). These properties may enable certain bacterial metabolisms. For example, Bosch et al. (2012) demonstrated that nano-sized (but not micron-sized) pyrite can be utilized by microbes as a source of sulfur for sulfur oxidation coupled to nitrate reduction. Additionally, thermodynamically metastable and potentially highly reactive metal sulfide phases may exist at the nano-scale, as demonstrated by the precipitation of wurtzite (hexagonal ZnS; Moreau et al., 2004; Xu et al., 2016) and α-NiS (Sitte et al. 2013) in low temperature biological systems. Empirical observations and calculations demonstrate that even at low abundances, NPs may be the most important component of a geochemical system as a result of their high reactivities (Hochella et al. 2012).

The reactivity and physicochemical attributes (size, morphology, phase, elemental compositions) of metal sulfide NPs are strongly affected by their formation mechanism(s). *Classical models* (e.g. Benning and Waychunas, 2008) describe formation via addition of simple ions (e.g. aqueous metals) until a sufficient density is reached to form a nucleus. This nucleus

tends to be a metastable phase that will dissolve and reprecipitate to form larger and more stable mineral phases in a process termed Ostwald ripening. In the past two decades, an alternative pathway for crystal formation in the form of *particle attachment* has come into light (reviewed by De Yoreo et al., 2015). Through this pathway, crystal nucleation and growth are mediated by attachment of smaller primary units, which may range from sub-nanometer sized aqueous clusters to NPs tens of nanometers in size. The particle attachment pathway tends to be dominant at high supersaturation when nucleation events are common (De Yoreo et al. 2015), a condition that is easily satisfied for metal sulfides due to their low solubilities (Rickard and Luther 2006). The nucleation of metal sulfides most likely results from assembly of aqueous clusters (e.g. Fe_2S_2, Cu_3S_3, Zn_3S_3 less than 1 nm in size; Luther and Rickard, 2005), followed by growth via oriented attachment of discrete nanocrystals (Pileni et al. 1997; Libert et al. 2003; Moreau et al. 2004; Schliehe et al. 2010; Mullaugh and Luther 2011; Xu et al. 2016). Misalignments during particle attachment may result in defects in the crystal structure, which contribute to the nanoparticle reactivity if the defects are not eliminated through recrystallization (Penn and Banfield 1998; Echigo et al. 2012; Eskelsen et al. 2018).

The physicochemical attributes of naturally-occurring metal sulfide NPs can greatly impact their roles in biogeochemical cycles. It is however challenging to characterize natural NPs due to their relatively low abundances and the current technical limitation in separating them from the environment (e.g. Lead and Wilkinson, 2006; Caraballo et al., 2015). Metal sulfide NPs also tend to be altered immediately in the presence of oxygen and thus requires strict anoxic sampling and storage procedures prior to analyses. To circumvent these challenges, metal sulfide NPs can instead be precipitated under specified and controlled laboratory conditions. A few generalizations can be made in order to aid experimental designs that yield results relevant to

natural settings. First, the majority of metal sulfides are precipitated in low temperature anoxic zones as a result of sulfate reduction metabolism by microorganisms (Berner 1984; Picard et al. 2016). Experiments have shown that besides supplying the sulfide source, the presence of microbial cell walls and extracellular organic compounds also play major roles in modifying the formation mechanism, size, shape, phase, solubility and aggregation state of the precipitates (Gramp et al. 2006, 2010; Moreau et al. 2007; Sitte et al. 2013; Xu et al. 2016; Picard et al. 2018). Second, natural metal sulfides precipitate in complex solution containing other inorganic metals, which may result in co-precipitation of mixed-metal sulfide NPs such as chalcopyrite ($CuFeS_2$; Hochella et al., 2005; Fulda et al., 2013; Gartman et al., 2014), Zn-Fe sulfides (Zbinden et al. 2001) and Cu-Cd-Pb sulfides (Hofacker et al. 2013). Some metal sulfides may also exist within pyrite grains as nano- to micro-sized inclusions (Large et al. 2014; Gregory et al. 2015). These mixed-metal sulfides will likely have different attributes and reactivities compared to single-metal sulfides, which highlights the need for systematic studies on their properties to better constrain their impacts to the environment. Furthermore, any characteristics that are unique to biogenic or abiogenic NPs can be used as biosignatures (Des Marais et al. 2008; Horneck et al. 2016) or to differentiate between natural (often biogenic) and engineered (often abiogenic) NPs that are increasingly being released to the environment (e.g. Nowack et al., 2012).

To this end, we conducted a study aiming to characterize the physicochemical attributes and formation mechanisms of Fe-Cu sulfide NPs precipitated under anoxic conditions in the presence and absence of sulfate reducing bacteria. X-ray diffraction (XRD) was used in conjunction with transmission electron microscopy (TEM)-based analyses such as selected area electron diffraction (SAED) and energy dispersive X-ray spectroscopy (EDS) to provide data at the bulk

sample and individual crystal scale, respectively. Depending on the initial aqueous Fe-to-Cu ratios, we find that either nanoparticulate mackinawite (FeS), covellite (CuS), chalcopyrite ($CuFeS_2$) and/or nukundamite ($Cu_{5.5}FeS_{6.5}$) is/are formed. Covellite NPs show significant variation in Fe content and morphology (fine-scale spheroids vs nanorods vs nanoplates) depending on the synthesis conditions and even within a single reaction system. The presence of defects in covellite with certain morphology implicates formation by particle attachment followed by potentially rapid recrystallization. Chalcopyrite formation is found to proceed through incorporation of Fe into precursor covellite NPs, which adds to the poorly understood pathway of low temperature chalcopyrite formation. The presence of bacteria modifies the crystal sizes, the phases formed (e.g. unique bio-greigite (Fe_3S_4) formation from mackinawite) and the selectivity of mineral precipitation (e.g. more chalcopyrite) compared to abiotic systems. We hypothesize that these changes are induced by precipitation within local microenvironments surrounding the bacterial cells with different chemistry compared to the bulk solution. To our best knowledge, the reported work is the first systematic study on mixed Fe-Cu sulfide NPs precipitated in low-temperature aqueous solutions that are similar to environments on the majority of the Earth's (sub)surface.

Background: Fe-Cu-sulfide mineral system

Iron sulfides such as mackinawite (tetragonal FeS), greigite (cubic Fe_3S_4) and pyrite (cubic FeS_2) are common constituents of low temperature anoxic environments on the Earth's (sub)surface (reviewed by Rickard and Luther, 2007). Multiple experiments have shown that the earliest phase precipitated during the reaction of Fe(II) with sulfide in aqueous solution is nanoparticulate mackinawite (e.g. Schoonen and Barnes, 1991; Harmandas and Koutsoukos,

1996; Herbert et al., 1998; Benning et al., 1999; Wolthers et al., 2003; Michel et al., 2005; Ohfuji and Rickard, 2006; Csákberényi-Malasics et al., 2012; Zhou et al., 2014; Picard et al., 2018). The nucleation of mackinawite is mediated by the assembly of sub-nanometer aqueous clusters in the form of Fe_2S_2, followed by crystal growth via aggregation and attachment of the nuclei (Luther and Rickard 2005). Iron isotopic studies support the growth of mackinawite through aggregation (Guilbaud et al. 2010), although direct observation of FeS particle attachment has not been observed to our knowledge. In the presence of either trace oxidants (e.g. oxygen, elemental sulfur, oxidized species on mineral surfaces), trace Ni, bacteria, acidic pH or high temperatures, mackinawite can be transformed into greigite and pyrite within days to weeks (Rickard 1975; Luther 1991; Harmandas et al. 1998; Benning et al. 2000; Rickard and Luther 2007; Gramp et al. 2010; Bourdoiseau et al. 2011; White et al. 2015; Morin et al. 2017; Wan et al. 2017; Picard et al. 2018). Mackinawite may also contain and adsorb significant amounts of trace metals such as Ni, Mn, Cu, Co and Zn, and likely play a key role in trace metal sequestration in the environment (e.g., Morse and Arakaki, 1993; Parkman et al., 1999; Veeramani et al., 2013; Zavašnik et al., 2014; Ikogou et al., 2017; Wilkin and Beak, 2017).

Copper sulfides in general are trace components in environments on the Earth's surface, except in environments exposed to effluents from Cu-rich mining sites (Weber et al., 2009b; Fulda et al., 2013; Hofacker et al., 2013). It is difficult to identify the exact phase(s) of Cu-sulfides present in nature as the Cu-S mineral system contains a variety of phases with variable Cu-to-S ratios, redox states and crystal structures (XRD patterns for each shown in Fig. S1). Experiments in low temperature aqueous solutions however indicate that covellite (hexagonal Cu(I)S) is the most common product (Gramp et al. 2006; Sampaio et al. 2009; da Costa et al. 2013; Ikkert et al. 2013). Similar to mackinawite, nucleation of Cu-sulfides is thought to result

from the assembly of aqueous clusters such as Cu_3S_3 and Cu_4S_6 (Luther et al., 2002; although see Ciglenečki et al., 2005 for a debate on the existence of Cu-sulfide clusters). Copper is typically supplied as the Cu^{2+} ion, which must undergo reduction to Cu^{+} prior to covellite formation. The reduction process occurs within minutes in the presence of sulfide (Pattrick et al. 1997; Luther et al. 2002). No TEM-based studies have yet been performed to determine the formation mechanism of covellite precipitated in low temperature aqueous solutions. Experiments done in high temperature organic solvents indicate that aggregation and attachment of the nuclei are likely the primary mechanism for crystal growth of various copper sulfide nanocrystals (Xu et al. 2006; Du et al. 2007; Zhang et al. 2008; Li et al. 2011).

The mixed Fe-Cu-sulfide mineral system is much less studied compared to pure Fe- or Cu-sulfide mineral system especially under low temperature aqueous conditions. There are several known mixed Fe-Cu-sulfide minerals ranging from the Fe-rich endmember of cubanite ($CuFe_2S_3$) to the Cu-rich endmember of nukundamite ($Cu_{5.5}FeS_{6.5}$) (XRD patterns for each shown in Fig. S2). Among these minerals, chalcopyrite ($CuFeS_2$) is arguably the most common phase on the Earth's (sub)surface. The oxidation states of Cu and Fe in chalcopyrite have been a subject of intense debate, although recent studies indicated Cu exists in the monovalent state (Cu^{+}) and Fe in the trivalent state (Fe^{3+}) (Boekema et al. 2004; Goh et al. 2006; Pearce et al. 2006; Klekovkina et al. 2014; Conejeros et al. 2015). Since the 1960s, there are a few studies focusing on the formation mechanism for chalcopyrite in low temperature aqueous solutions. Roberts (1961) formed chalcopyrite by attaching thin blocks of pyrrhotite ($Fe_{1-x}S$; $x < 0.2$) and covellite together, prompting the suggestion that chalcopyrite was formed via solid state diffusion of Fe into covellite. Later on, Roberts (1963) formed chalcopyrite by mixing equimolar amount of aqueous Fe and Cu with excess sulfide. On the basis of the fast reaction rate on the

order of minutes, he revised his earlier hypothesis and concluded that chalcopyrite formation must proceed through aqueous-mediated recrystallization of Fe- and/or Cu-sulfides. Cowper and Rickard (1989) repeated Roberts' earlier experiments and found contradictory results. In the presence of excess sulfide, they did not form chalcopyrite either by reacting (i) solid Fe-sulfides + solid Cu-sulfides, (ii) aqueous Fe + aqueous Cu, or (iii) aqueous Fe + solid Cu-sulfides. The only reaction capable of forming chalcopyrite was through the addition of aqueous Cu to solid Fe-sulfides. They therefore concluded that chalcopyrite can only form through reactions between aqueous Cu and a precursor Fe-sulfide mineral, consistent with the formation of Fe-sulfide phases prior to chalcopyrite formation in later studies (Parkman et al. 1999; Karnachuk et al. 2008; Ikkert et al. 2013).

Materials and Methods

The experiments were performed at (i) different initial aqueous Fe-to-Cu ratios ($M_{Fe/Cu}$) and (ii) in the presence and absence of sulfate reducing bacteria in order to systematically study the factors controlling the formation of mixed-metal sulfide NPs. All experiments were performed in acid-cleaned serum vials to prevent trace metal carry-overs. Sample preparation and experimental procedures were conducted under anoxic conditions unless otherwise specified. Anoxic solutions were prepared by boiling for 20 min and N_2 degassing for another 20 minutes, followed by storage under pure N_2 or N_2/H_2 (97%/3%) headspace. A modified metal toxicity medium (MTM) was used as the precipitation matrix, which contains (per liter): 3.8 ml 80% lactic acid, 2.23 g Na_2SO_4, 0.06g $CaCl_2.2H_2O$, 1.0 g NH_4Cl, 1.0 g $MgSO_4.7H_2O$, 0.05 g yeast extract, 0.5 g tryptone and 2.83 g HEPES. Initial pH was adjusted to 7.2 by the addition of

NaOH. Metal stock solutions were prepared separately as 20 mM $CuCl_2.2H_2O$ or 10 mM $FeSO_4.7H_2O$ (the latter in pH 2 HCl solution matrix to prevent oxidation) and then later added into the medium. Five different systems with variable $M_{Fe/Cu}$ were tested: 1:0 (that is, 1,000 μM Fe with no added Cu), 2:1, 1:1, 1:5 and 0:1 (500 μM Cu with no added Fe). The mixed metal systems were prepared either by keeping the Cu concentration constant at 500 μM while varying the Fe concentrations, or by maintaining a constant total metal concentration of 500 μM. The resultant precipitates were collected for analyses after 4 to 30 days of incubation. Long-term changes were also monitored by collecting precipitates after up to 6 months of incubation.

Bacterial cell cultures and biological precipitation

Biological precipitation experiments were conducted by utilizing the sulfate reduction metabolism of *Desulfovibrio vulgaris* strain DSM 644 (also known as ATCC 29579 or strain Hildenborough) as a gradual sulfide source. The culture was maintained at either 4°C or 30°C over a period of weeks to months in modified Postgate medium (DMSZ medium #63; media composition detailed in Xu et al., 2016). Prior to each precipitation experiments, the culture was inoculated at 1% v/v into MTM and allowed to grow for 72 hours at 30°C while shaking. This step was crucial to remove metals that might be carried over from the Fe-rich Postgate medium. Sulfide concentrations were monitored through the methylene blue assay (Hach Co., CO, USA) at this stage and reached a maximum of 15 mM after 3 days. The cells were then inoculated at 1% v/v into 100 ml of metal-amended MTM for the actual precipitation experiments. Within a day of incubation at 30°C while shaking, black or dark brownish metal sulfide precipitates formed in the cultures, and each sample was separated into two aliquots for XRD (~80 ml) and

TEM (~5 ml) analyses. Precipitates were first pelleted by centrifugation at 15,000*g* for 5 min. Pellets for XRD were washed once with 10 ml anoxic H_2O prior to being resuspended in ~0.8 ml of anoxic H_2O and allowed to dry on a glass slide as a thin film. Pellets for TEM were treated with 10 ml of anoxic 0.1% Triton-X solution containing lysozyme and proteinase K (100 µg/ml of each) for 1 hour at 45°C to lyse associated bacterial cells, which were then removed from the NP fraction by centrifugation at 15,000g for 15 min. The NPs were washed once with 10 ml anoxic H_2O before being set aside for TEM analyses.

Abiotic precipitation

Abiogenic metal sulfide NPs were precipitated through titration of 50 ml of 15 mM $Na_2S.9H_2O$ (in MTM matrix, pH 7.2) into 50 ml of metal-amended MTM at a rate of 2 ml/hr inside the anaerobic chamber. The solutions were kept well-mixed using a Teflon-coated magnetic stir bar. At the end of the titration, the stir bar was removed to prevent nucleation/growth effect due to added surface areas. Aggregates of NPs were separated by filtration through a 0.2 µm pore size mixed cellulose ester membrane; the solution remained clear during this step. The NP residues were then resuspended in 1 ml anoxic H_2O through repeated mixing by a pipettor. Approximately 0.8 ml of each sample was dried onto a glass slide for XRD analyses, while the rest was stored in H_2O until being prepared for TEM analyses.

Characterization

X-ray diffraction patterns of precipitates were collected using a Rigaku Miniflex II equipped with a Cu Kα source. Individual scans were collected from 10 to 60° 2θ angle with a step size of

0.05° and scan speed of 0.25°/min, totaling a collection time of ~3.3 hours per sample. Background correction was performed manually in Jade software using a scan collected from a blank glass slide as reference. Average crystal size (L) along a plane was estimated using the Scherrer equation:

$$L = K \lambda / (\beta \cos \theta) \quad (1)$$

where K is the Scherrer shape constant (assumed to be 0.9; Langford and Wilson, 1978), λ is the X-ray wavelength (0.15418 nm for Cu Kα), β is the full width half maximum (FWHM) of a peak corresponding to a particular plane and θ is the angle position of a peak. Intrinsic instrument broadening can contribute to error in β. This error was estimated by comparison to a commercial copper oxide nanoparticle (product #544868 from Sigma Aldrich) with known XRD-derived crystal sizes of 18 nm (Triboulet et al. 2015). From this analysis, measurement errors contributed by β are expected to be < 1 nm for crystal sizes under 10 nm.

Samples for TEM analyses were prepared in the anaerobic chamber by diluting in anoxic H_2O followed by sonication for up to one hour to disperse any aggregates. Between 2.5 and 10 µl of dispersed samples were dried onto Ni-coated grids (HC200-Ni, Electron Microscopy Sciences, PA, USA) and shipped in an anoxic container (SampleSaver^{TM} Storage Container, model SS-100/200, South Bay Technology Inc., CA, USA) to the NanoEarth facility at Virginia Tech. Samples were imaged within two weeks of shipping using a JEOL-2100 TEM operating at 200 kV. There were no observable differences between samples that were dried immediately on the TEM grids and samples that were stored in anoxic H_2O for a few months prior to drying.

Elemental ratios (e.g. sulfur/metal) were measured with energy dispersive X-ray spectroscopy (EDS) with a silicon drift detector and quantified using the standardless analysis

295 method (Newbury and Ritchie, 2014). EDS spot analysis was conducted with a beam size of 20-
296 500 nm in diameter, while mapping analysis was conducted in scanning-TEM (STEM) mode
297 with a beam size of 3-10 nm. Samples exhibiting oxygen peaks that were higher than the grid
298 background (i.e., indicative of oxidation) were discarded from interpretation. D-spacing values
299 for NPs were measured on selected area electron diffraction patterns (SAED) in
300 DigitalMicrograph software. In high-resolution images where lattice fringes were clearly visible,
301 d-spacing values were also measured directly by averaging several interplanar distances or in
302 reciprocal space, based on the patterns derived after applying Fast Fourier Transform (FFT) in
303 Digital Micrograph. These methods gave d-spacing values that were consistent within ± 0.05 Å.

304

305 **Results & Discussion**

306 The metal sulfide NPs precipitated in this study display significant variations in their phase,
307 morphology and elemental compositions, primarily as a function of the initial aqueous Fe-to-Cu
308 ratios ($M_{Fe/Cu}$). In the following sections, we first describe the physicochemical attributes of these
309 NPs under each of the tested conditions. The formation mechanism(s) associated with these NPs
310 in single-metal systems, and how such mechanisms may be modified in mixed-metal systems,
311 are discussed. Additionally, the subtle differences in biogenic and abiogenic NPs are detailed and
312 the specific biological mechanisms causing these differences are proposed. Finally, the
313 physicochemical attributes of the synthetic NPs in this study are compared to those of naturally-
314 occurring NPs to ascertain if experimental approaches can be utilized to gain insight into NP-
315 mediated reactions in the natural biogeochemical cycling of metals and sulfur.

316

Initial Fe-to-Cu ratios as the primary control on the physicochemical attributes of biogenic and abiogenic nanoparticles

At 1:0 $M_{Fe/Cu}$ (Fe with no added Cu), mackinawite is the only phase detectable by XRD within 30 days of incubation. Both biogenic and abiogenic precipitates display a prominent XRD peak at 2θ angle of ~17° corresponding to the (001) plane of mackinawite (Fig. 1a). Estimated crystal sizes based on the (001) XRD peak indicate slightly larger biogenic mackinawite (7 to 9 nm) than abiogenic mackinawite (4 to 6 nm) (Table 1). All other peaks are either small or broad, consistent with the nanoparticulate nature of the precipitates. Under TEM, both abiogenic and biogenic mackinawite are observed to adopt wrinkled nanosheet morphology ~300 to 1,000 nm in size (Fig. 2a). This morphology is similar to mackinawite aggregates precipitated in other experimental studies (Ohfuji and Rickard 2006; Csákberényi-Malasics et al. 2012; Veeramani et al. 2013; Picard et al. 2018). Close observations of the nanosheets reveal electron dense, fibrous-like structures with d-spacing of 5.04 Å (Fig. 2b-c), corresponding to the (001) planes of mackinawite (Lennie, 1995; Table 2). These areas are interpreted to reflect regions where the nanosheet can be viewed edge-on, in cross-section, revealing the (001) plane. The SAED patterns derived from the nanosheets show diffuse rings with d-spacing values that corresponded to the (200), (111), (002) and (101) planes of mackinawite (Fig. 2d). The (001) diffraction ring, if present, is difficult to see due to its proximity to the high intensity (000) center spot. After six months of incubation, mackinawite remains as the sole material detectable by XRD with no significant change in the crystal sizes. Interestingly, TEM observations reveal minor amounts of 30-50 nm nanoplates in the biological systems that are absent in abiotic systems. Analysis of the SAED patterns derived from these nanoplates show that they are single crystals of greigite (Fig. 3a-b) or greigite aggregated with mackinawite (Fig. 3c-d).

At 0:1 $M_{Fe/Cu}$ (Cu with no added Fe), covellite is the only phase detectable by XRD for both biogenic and abiogenic precipitates, with higher crystallinity associated with the latter (Fig. 1b). Three morphologies of NPs are observed for both abiogenic and biogenic samples: fine nanocrystals < 10 nm in size (Fig. 2e), ~35 nm long nanorods (Fig. 2f) and ~40 nm wide nanoplates with poorly-defined edges (Fig. 2f-g). The SAED patterns collected from aggregates of the fine nanocrystals and nanoplates show diffuse rings as well as distinct diffraction spots with overlapping d-spacing values that are consistent with covellite (Fig. 2h; Table 2). Similarly, elemental S-to-Cu ratios (via EDS) of the nanorods and nanoplates indicate a ratio of 1.0 ± 0.1 (n = 2 each), consistent with covellite. However, the fine nanocrystals occasionally display excess S relative to Cu (up to S/Cu = 1.5), which could be due to sulfur adsorption to the NPs' surface or trace quantities of villamaninite (CuS_2).

High-resolution TEM images of both biogenic and abiogenic covellite nanorods reveal lattice fringes perpendicular to the elongation direction, with d-spacing values that correspond to either the (102) or (103) plane (Fig. 3e-g). All of the imaged nanorods display electron dense regions that we interpret to indicate randomly-located defects within the crystal structures. Depending on the orientation of the nanorods with respect to the electron beam, we can observe that some nanorods display clear defects in the form of atomic dislocations (Fig. 3h). For these defect-containing nanorods, the measured d-spacing (perpendicular to the elongation direction) vary from 2.82-2.95 Å; this value range falls in between the (102) and (103) plane (optimal d-spacing of 3.05 and 2.82 Å respectively; Table 2). Meanwhile, covellite nanoplates in the same sample are observed to be single crystals with no visible defects within the crystal structure; d-spacing analyses indicate a prominence of the (110), (102), (103) and (100) planes depending on the viewing orientation (Fig. 3i-l).

In mixed-metal systems, the physicochemical attributes of the precipitates are dependent on the $M_{Fe/Cu}$ but are not influenced by the total metal concentrations within the studied range. At 1:5 $M_{Fe/Cu}$, the XRD data for the abiogenic precipitates indicate covellite as the sole precipitate. In contrast, the XRD data for the biogenic precipitates indicate the presence of covellite along with another phase that resulted in a more intense peak at 28° 2θ angle (Fig. 1c). TEM analyses for both abiogenic and biogenic samples indicate the presence of NPs with morphological similarity to fine covellite nanocrystals, nanorods and nanoplates, along with the additional occurrence of larger (100-200 nm) and thick euhedral crystals with well-developed edges (Fig. 2i-l). Based on EDS, the large euhedral crystals contain Fe incorporated within its structure (Fig. 4a) and display average Fe/(Fe/+Cu) ratio of 0.11 ± 0.05 and S/(Fe+Cu) ratio of 0.92 ± 0.09 (n = 8). The elemental ratios are consistent with either Fe-rich covellite (Fe/(Fe+Cu) ratio of 0.01-0.18; Clark, 1971; Maydagán et al., 2013; Melekestseva et al., 2017) or nukundamite (hexagonal $Cu_{5.5}FeS_{6.5}$, Fe/(Fe/+Cu) = 0.15; Rice et al., 1979). Comparison of SAED patterns collected from the biogenic and abiogenic euhedral crystals indicates one major difference between the two. While abiogenic crystals display diffraction patterns with d-spacing values that are consistent with covellite (Fig. 2l), the biogenic crystals display an additional diffraction spot/ring corresponding to a d-spacing value around 3.15 Å (Fig. 3q-t); this d-spacing corresponds to the (101) plane of nukundamite with a corresponding 28° 2θ angle in XRD spectrum (Sugaki et al. 1981). Thus, abiogenic precipitates are composed of Fe-rich covellite while biogenic precipitates are composed of mixtures of Fe-rich covellite and nukundamite.

At 1:1 $M_{Fe/Cu}$, XRD data indicate the formation of chalcopyrite ($CuFeS_2$) in both biological and abiotic systems. In addition, smaller XRD peaks indicative of mackinawite and possibly nukundamite are also present in the abiotic system (Fig. 1d). High-resolution TEM analysis of

386 both biogenic and abiogenic precipitates show aggregates of 3 to 12 nm crystals with SAED-
387 derived d-spacing values of 3.07 and 1.89 Å (Fig. 2m, o-p), which can be attributed to either
388 chalcopyrite's (112) and (220)/(204) planes or to covellite's (102) and (103) planes (Table 2).
389 Elemental mapping of the nanocrystal aggregates indicates overlapping distributions of Fe, Cu
390 and S with approximate ratios of 1:1:2 (Fig. 4b). Based on the XRD, EDS and SAED data, we
391 therefore identify the nanocrystal aggregates as chalcopyrite. Close observations also reveal the
392 presence of nanorods (in both the biological and abiotic systems) and nanoplates (in biological
393 system only) that are morphologically similar to covellite precipitated in the absence of Fe (Fig.
394 2n, Fig. 5). Based on EDS, the nanorods and nanoplates display a wide range of Fe/(Fe+Cu)
395 ratios (0.04 to 0.43; average 0.26 ± 0.15) and S/(Fe+Cu) ratios (range of 0.74 to 1.11; average =
396 1.00 ± 0.11). The SAED patterns derived specifically from the nanoplates and nanorods yield d-
397 spacing values that are consistent with chalcopyrite, nukundamite and covellite; these crystals
398 likely represent a variety of Fe-Cu-S minerals with variable crystal chemistry and elemental
399 compositions similar to chalcopyrite at one end and covellite at the other.

400 At 2:1 $M_{Fe/Cu}$, chalcopyrite is the main precipitate detected by XRD along with lesser
401 amounts of mackinawite in both biological and abiotic systems (Fig. 1e). The chalcopyrite
402 nanocrystals were similar in morphology to the nanocrystal aggregates observed at 1:1 $M_{Fe/Cu}$
403 (Fig. 2q-s). No nanorods or nanoplates are observable. Collected SAED patterns from the
404 nanocrystal aggregates display diffuse rings with d-spacing values of 3.07 and 1.88 Å
405 corresponding to the (112) and (204) planes of chalcopyrite (Fig. 2t). Although the presence of
406 mackinawite is indicated by XRD data, no images of mackinawite are captured by TEM.

407 Aged precipitates from the pure Cu or mixed Fe-Cu systems are examined up to four months
408 following the initial precipitation to determine if the NPs evolve significantly over time. Aging

409 does not cause variation in the bulk XRD data, indicating that most nucleation and growth
410 occurred within the first few days and stopped after the aqueous metal supply is exhausted due to
411 excess sulfide production or addition. Under TEM, small changes in crystal sizes over time are
412 discernible. Specifically, biogenic covellite nanoplates precipitated at 0:1 $M_{Fe/Cu}$ decrease slightly
413 in size over a period of 50 days, while the size of the nanorods remain unchanged (Fig. S3).
414 These changes are not studied systematically for all samples and are beyond the scope of the
415 current study.

416

417 **Formation mechanism(s) of Fe-Cu-sulfide nanoparticles**

418 The final size, morphology and elemental composition of the metal sulfide NPs, be it
419 mackinawite, covellite or chalcopyrite, vary significantly depending on the initial aqueous Fe:Cu
420 ratios, both in the absence and presence of *D. vulgaris*. These variations in physicochemical
421 attributes likely stem from fundamental changes in the formation mechanism(s) of the respective
422 NPs caused by precipitation in the presence of other metal ions, as discussed below.

423

424 **Mackinawite: size modification in the presence of Cu.**

425 In our study, we find that smaller mackinawite NPs are formed in both biogenic and
426 abiogenic systems when precipitation occurred in the presence of Cu (Table 1; compare $M_{Fe/Cu}$ =
427 2:1 and 1:1 versus $M_{Fe/Cu}$ = 1:0). This result is in contrast to the study by Zavašnik et al. (2014)
428 who found larger mackinawite NPs when precipitation occurred in the presence of Cu. Density
429 functional theory simulations by Kwon et al. (2015) support the results of Zavašnik et al. (2014)
430 and further attribute the change to the substitution of Cu for Fe in mackinawite's crystal

structure, leading to an increase in d-spacing along the (001) plane. Thus, we also measure the (001) d-spacing based on our XRD data and find that while abiogenic mackinawite display increased (001) d-spacing (consistent with previous results), biogenic mackinawite actually display smaller (001) d-spacing in the presence of Cu. This implies that differences in the experimental setup and/or biological effects can possibly modify the exchange mechanism between Fe and Cu ions in mackinawite as well as the incorporation of Cu into the space between the (001) planes, leading to differences in the particle size. Such changes may have implications to mackinawite's reactivity and stability (Kwon et al. 2015), and further investigation is necessary to illuminate the specific mechanism.

Covellite: the role of particle attachment and Fe in promoting growth.

In this study, covellite show remarkable variation in terms of morphology, from fine nanocrystals, nanorods, and nanoplates, to larger and thicker Fe-rich crystals of up to 200 nm in size. Because of covellite's exceedingly low solubility (Shea and Helz 1989) and rapid nucleation kinetics (Morse and Luther 1999), crystal growth via particle attachment was proposed to be its dominant growth mechanism (Luther and Rickard 2005; Rickard and Luther 2006). This is in part supported by previous TEM analyses showing oriented attachment of covellite nanorods (Xu et al. 2006) and nanoplates (Du et al. 2007) and other Cu-sulfide phases (Li et al. 2011). In the current study, direct observations of oriented attachments for covellite nanostructures are however uncommon. One example of such observation is seen for precipitates at day 4, whereby ~3-5 nm nanocrystals are oriented to form a larger pseudo-nanorod structure (Fig. 6). Aside from this example, TEM analyses also indicate aggregation of nanorods and stacking of smaller nanoplates and nanocrystals on top of larger nanoplates (Fig. S4), although it

454 is unclear if these are the natural state of the NPs or an artifact of sample preparation. The
455 absence of strong evidence for oriented attachment may implicate either classical ion-by-ion
456 growth or fast recrystallization of covellite NPs following initial particle attachment. For the
457 latter mechanism, we note that previous studies performed TEM analysis within 24 hours of
458 initial covellite precipitation (Xu et al. 2006; Du et al. 2007; Li et al. 2011), compared to the
459 longer (i.e., $\geq$ 4 days) duration in the current study. It is possible for covellite recrystallization to
460 occur within this period based on its fast nucleation kinetics, leading to the erasure of any
461 evidence for oriented attachment prior to TEM analysis of the samples.

462 Indirect evidences for particle attachment formation pathway of covellite can be seen in the
463 forms of defects within the NPs' structures. At 0:1 and 1:5 $M_{Fe/Cu}$, stacking faults and/or
464 twinning are observable in the fine covellite nanocrystals and nanorods. Defects within the fine
465 nanocrystals developed along either the (100)/(101) (measured d-spacing cannot conclusively
466 differentiate between the two) or (102) plane (Fig. 7a-c) while defects within the nanorods
467 developed along the (102) or (103) plane (Fig 3e-h; Fig. 7d-e). It is particularly noted that these
468 structural defects are associated with most of the observed nanorods. The occurrence of the (102)
469 planes in the fine nanocrystals and nanorods is unexpected given the relatively high energies of
470 these surfaces (Morales-García et al. 2017). We predict that the surface energies of the (101) and
471 (103) planes should be similarly high in energy, although this remains to be confirmed. Based on
472 these, we establish a positive relationship between the occurrence of structural defects and the
473 exposure of high-energy planes of covellite. Two possible mechanisms might have led to the
474 occurrence of structural defects. The first mechanism is through crystallographic attachment of
475 sub-nanoparticles along (i.e., to hide) the high-energy planes. In this case, twinning and stacking
476 faults could have been formed due to a relatively high probability of imperfect lattice matching

of two (101)/(102)/(103) surfaces coming together. The second mechanism relates to the release of the relatively high energy associated with the (101)/(102)/(103) surface through formation of structural defects (as has been explained in the case of ZnS in Xu et al., 2016). Structural defects are however absent in the hexagonal nanoplates (including in the Fe-rich euhedral plates), consistent with this morphology being the predicted equilibrium morphology of covellite (Morales-García et al. 2017). The absence of defects in these nanoplates most likely indicate rapid recrystallization to a thermodynamically stable morphology. Overall, TEM data seem to confirm the growth via attachment and re-assembly of sub-nanoparticles as the dominant mechanism for the formation of defects in the fine nanocrystals and nanorods.

The addition of Fe leads to the formation of euhedral covellite crystals up to 200 nm in size. To our knowledge, this is the first recognition of Fe promoting covellite's crystal growth. One explanation is that the incorporation of Fe into covellite's crystal structure results in a higher thermodynamic stability for the mineral, thus allowing growth to larger sizes at equilibrium. Another possibility, assuming growth by particle attachment, is that Fe adsorption to the covellite surface weakens the repulsion between covellite NPs and allows more attachment events to occur. Regardless of the specific mechanism, our study conclusively demonstrated that the addition of a foreign metal ion can significantly modify the size and morphology of metal sulfide NPs, which likely affects the reactivity of these NPs.

Chalcopyrite and nukundamite: Formation via Fe incorporation into precursor covellite.

The formation of chalcopyrite at low temperature was previously claimed to proceed predominantly, if not exclusively, through incorporation of Cu into precursor Fe-sulfides (Cowper and Rickard 1989). However, in this study we are able to form chalcopyrite by adding excess sulfide to aqueous mixtures of Fe and Cu (at 2:1 and 1:1 $M_{Fe/Cu}$), consistent with the earlier work of Roberts (1963). Cowper and Rickard (1989) performed a similar experiment and found that the "immediate" precipitates were poorly crystalline mackinawite, yarrowite ($Cu_{1.12}S$), spionkopite ($Cu_{1.39}S$) and additional XRD-invisible phases with variable Fe/Cu ratios. Aged precipitates were not analyzed in that study. We analyze the early-phase abiogenic precipitates (~3 hours old) produced at 1:1 $M_{Fe/Cu}$ in our study and find no XRD-detectable phases. Thus, it seems that abiogenic chalcopyrite formation requires > 3 hours of aging, which may explain why it was not detected in the earlier work of Cowper and Rickard (1989). In our study, this same experimental design yields mixed Fe-Cu-containing nanocrystals, nanorods and nanoplates that are morphologically similar to covellite after four days of aging (Fig. 2n), suggesting that chalcopyrite (and nukundamite) is formed through incorporation of Fe into precursor covellite. This is consistent with the notion that covellite should form faster than Fe-sulfides (Morse and Luther 1999). Additionally, chalcopyrite formation had been shown to proceed through incorporation of aqueous Fe into Cu-sulfides at high temperatures (> 100°C), with the morphology of the precursor Cu-sulfides being preserved during the reaction (Liu et al. 2018). To confirm whether this same reaction pathway can proceed at low temperatures, we add 500 μM of aqueous Fe to a 500 μM covellite suspension in MTM (previously aged for six days) and allow the reaction to proceed for four days at room temperature in the presence of excess sulfide (~7 mM). The final precipitates are identified by XRD as chalcopyrite, nukundamite and mackinawite with no traces of covellite remaining. This result confirms that chalcopyrite can

form through incorporation of Fe into precursor covellite. The discrepancy with the earlier work of Cowper and Rickard (1989) most likely stems from the use of polished sections of highly crystalline Cu-sulfides compared to the use of covellite NPs in the current study, which highlights the stark difference in reactivity for nano-scale versus larger-scale minerals.

Bacterial presence influences the crystal sizes and phase selectivity of Fe-Cu-sulfide NPs

The presence and metabolic activity of sulfate reducing bacteria (SRB) can influence Fe-Cu-sulfide NPs precipitation in our study in several ways. The cell walls of bacteria and secreted extracellular polymeric compounds (EPS) contain anionic carboxyl and phosphoryl groups, which allows for the adsorption of positively charged Fe and Cu ions (Beveridge and Murray 1976; Beveridge and Koval 1981; Ferris et al. 1989; Chen et al. 2011; Hao et al. 2013). As SRB produce sulfide, metal sulfide NPs are preferentially precipitated on the cell walls and EPS, as previously documented for Fe-sulfides (e.g., Fortin et al., 1994; Herbert et al., 1998; Donald and Southam, 1999; Picard et al., 2018) and Cu-sulfides (Jalali and Baldwin 2000; Kiran et al. 2015). Once these NPs are formed, interactions with organic molecule assemblage secreted by SRB can further modify the NPs' properties. For example, organic coatings can bridge the interaction between two or more NPs and encourage growth via aggregation, or conversely inhibit growth by coating the NPs (Ikuma et al. 2015). The properties of the biogenic NPs are therefore potentially influenced by the complex interaction between various organic molecules with the metal ions and the nanoparticle surfaces.

Mineral-specific response to biologically-mediated crystal size modification.

In our study, we observe a significant difference in the crystal size/crystallinity (based on XRD) of the biogenic NPs compared to abiogenic NPs. Specifically, biogenic mackinawite exhibits larger crystal sizes (Table 1; Fig. 1a) while biogenic covellite exhibits lower crystallinity compared to their abiogenic counterparts (Fig. 1b). No significant size differences are found between biogenic and abiogenic chalcopyrite, although its formation in a complex mineral mixture makes comparison difficult. Overall, the results are consistent with previous studies that compare between biogenic and abiogenic mackinawite (Gramp et al. 2010; Picard et al. 2018) and covellite (Gramp et al. 2006). Differences in precipitation rates were considered as a potential mechanism to explain these size differences, although studies on FeS and ZnS found no correlation between precipitation rates and crystal sizes (Xu et al. 2016; Picard et al. 2018). For biogenic mackinawite, its size increase was attributed to the presence of cell walls and EPS that acted as nucleation and growth sites for the mineral (Picard et al. 2018). The contrasting size response of biogenic covellite compared to biogenic mackinawite indicate a complex interaction between bacteria and NPs, with size modification effects to the NPs that are mineral-specific.

Greigite and chalcopyrite formation favored via precipitation on the cell wall and EPS.

In the presence of SRB, mackinawite is observed to transform to greigite after six months of incubation in the absence of Cu. This transformation process requires the oxidation of mackinawite to Fe(III)-containing mackinawite, which acts as an intermediate for greigite formation (Bourdoiseau et al. 2011; White et al. 2015). Trace amounts of oxygen introduced during sample handling may accelerate this reaction, resulting in artefactual greigite formation that is not representative of experimental conditions (Rickard and Luther 2007; Csákberényi-Malasics et al. 2012). We note that oxygen contamination is unlikely in this study given that all

samples are handled anoxically as much as possible. Furthermore, greigite is only observed in the six months old biogenic sample and not for any other samples. Disregarding oxygen as a potential oxidant, H^+ is the most likely oxidant for the transformation reaction, as originally proposed by Rickard and Luther (2007). This idea is consistent with the observations that greigite formation from mackinawite proceeded slowly at near-neutral pH but was significantly accelerated at acidic pH (Bourdoiseau et al. 2011). With this in mind, we can propose that the role of SRB is to provide low pH (sub)micro-environments that help to catalyze greigite formation. It is well established in a variety of microbial biofilms that low pH microenvironments around cells can be generated due to secretion of inorganic and organic acids, even in well-mixed reactors (De Los Ríos et al. 2003; Hunter and Beveridge 2005; Hidalgo et al. 2009). Specific to *D. vulgaris*, sulfate reduction is coupled to lactate breakdown to acetate (Pankhania et al. 1986; Voordouw 2002; Heidelberg et al. 2004), which generates acidity (H^+) around the cells:

$$2\ C_2H_4OHCOO^- + SO_4^{2-} \rightarrow 2\ CH_3COO^- + 2\ HCO_3^- + HS^- + H^+ \quad (2)$$

This hypothesis can be tested by comparative analysis of NPs associated with the cell surfaces versus those located further away, possibly via (i) sample embedding coupled to cryo-electron microscopy to preserve spatial information as much as possible or (ii) pre-separation of the different NP fractions based on size and/or density. In both cases, the possibility of NPs being detached from the cell surfaces during sample preparation must be taken into account. While challenging, research into this area may provide new insights into unrecognized pathways for Fe redox cycling in anoxic environments.

In mixed-metal systems, the presence of SRB selectively favors the precipitation of nukundamite and chalcopyrite at lower $M_{Fe/Cu}$ compared to abiotic systems. Specifically, at 1:5

589 $M_{Fe/Cu}$, biological system produces nukundamite at sufficiently high abundance for XRD
590 detection while abiotic system only produces Fe-rich covellite. Additionally, at 1:1 $M_{Fe/Cu}$,
591 biogenic chalcopyrite is detected as the dominant phase by XRD, while abiotic system produced
592 a mixture of chalcopyrite, mackinawite and nukundamite. These observations indicate that the
593 presence of SRB accelerate the rearrangements of atoms to form mixed Fe-Cu-sulfide NPs with
594 crystal structures that are distinct from the precursor covellite (with some Fe substituting for Cu
595 within the crystal structure). The overall reaction for covellite (copper(I) sulfide) transformation
596 to chalcopyrite (copper(I)-iron(III)-sulfide) is given by:

597 $$CuS_{(s)} + Fe^{2+} + HS^- \rightarrow CuFeS_{2(s)} + H^+ \quad (3)$$

598 As written, the sulfur atom in covellite and aqueous Fe participates in a redox reaction, with the
599 former acting as an oxidant. The sulfur atom associated with bisulfide provides the additional
600 sulfur to form chalcopyrite without participating in redox reactions. The overall reaction
601 indicates that chalcopyrite formation is preferred in areas where high amounts of covellite, Fe
602 and sulfide are available, as typically found around bacterial cells and associated EPS. The
603 transformation reaction produces H^+ as a by-product that can potentially be harvested by SRB to
604 supplement proton gradient maintenance across cell membrane for ATP generation, similar to as
605 proposed for the function of intracellular calcite precipitation in *Achromatium* (Mansor et al.
606 2015). Overall, we postulate that the presence and metabolic activities of SRB play a major role
607 in accelerating the formation of chalcopyrite and nukundamite from covellite.

608

609 **Environmental Implications**

Because of the technical challenges in isolating and characterizing naturally-occurring NPs, there is a huge interest in using synthetic NPs to gain insight into the behavior of natural NPs, which may prove fruitful as long as these two types of NPs share the same physicochemical attributes. We therefore perform a literature search of electron microscopy-based studies on metal sulfide NPs found in low temperature environments for comparison with our synthetic NPs. Notably, ~20 nm mackinawite nanorods from the riverbeds of the Clarence River (Australia) (Burton et al. 2009), 2-35 nm spherical covellite, anilite ($Cu_{1.75}S$) and chalcocite (Cu_2S) in organic-rich soils contaminated by mining activities in Ontario (Canada) (Mantha et al. 2019), ~100 nm aggregates of < 10 nm chalcopyrite NPs from riverbeds of the Clark Fork River Superfund Complex (USA) (Hochella et al. 2005) and ≤ 50 nm chalcopyrite spheroids in hydrothermal emissions from the Mid-Atlantic Ridge (Gartman et al. 2014) are similar in size and morphology to the synthetic NPs in our study. In contrast, 100-200 nm mackinawite nanorods and 400-500 nm greigite nanoplates found in the Yangtze Estuary sediments (Niu et al. 2018) and 10-20 μm euhedral crystals of covellite observed in Whipsaw Creek, British Columbia (Canada) (Lett and Fletcher 1980) are distinctly larger than any NPs in our study. Overall, these comparisons indicate that laboratory experiments can form metal sulfides that have similar size and morphology to natural precipitates in some environments.

It is clear from our study that under any conditions akin to complex environmental systems, a mixture of metal sulfide NPs with variable physicochemical attributes will be produced. This will be especially true in dynamic environments when the ratio of metals can vary due to external factors (variable supply rate or solubility due to changes in redox) or even as competing precipitation reactions progress at different rates. The presence of bacteria and associated extracellular compounds further act to concentrate reaction zones and to encourage the formation

633 of mixed-metal sulfides with distinct crystal structures, but do not display any overt features that
634 can be used to distinguish biogenicity (at least for Fe-Cu-sulfide NPs). We therefore expect
635 metal sulfide NPs to be extremely diverse even over small sampling scales.

636 The properties of the precipitated metal sulfide NPs greatly affect their reactivity, stability
637 and transport properties with implications relevant to heavy metal immobilization and release to
638 surrounding waters. As a general rule for single phase (or metal) systems, smaller crystals will
639 have the highest surface area normalized reactivity and may dominate geochemical reactions. In
640 mixed-metal systems, one also needs to consider the formation of different phases with different
641 solubilities (chalcopyrite vs nukundamite vs covellite for Cu; mackinawite vs Cu-rich
642 mackinawite for Fe). Additionally, the incorporation of foreign metals may cause defects and
643 size modifications to the crystal structure that can potentially enhance or lower reaction rates,
644 especially for NPs. Future dissolution and bio-availability studies on NPs generated from mixed-
645 metal systems will greatly help in identifying the most reactive component(s) that may also point
646 to the main driver of geochemical reactions in nature.

647

648 Acknowledgements

649 This work was funded by the grant DOE-BES DE-FG02-06ER15786 awarded by the
650 Department of Energy to Mike Hochella, Mitsu Murayama and Jie Xu and by the start-up grant
651 to Jie Xu by the University of Texas at El Paso. This work uses shared facilities at the Virginia
652 Tech National Center for Earth and Environmental Nanotechnology Infrastructure (NanoEarth),
653 a member of the National Nanotechnology Coordinated Infrastructure (NNCI) network,
654 supported by NSF (NNCI 1542100). NanoEarth is housed at Virginia Tech's Institute for Critical

655 Technology and Applied Sciences (ICTAS). We thank the associate editor, Andrew Madden and
656 an anonymous reviewer for helpful comments that improved the manuscript.

657

658 **References**

659 Banfield, J.F., and Zhang, H. (2001) Nanoparticles in the environment. Reviews in Mineralogy
660 and Geochemistry, 44, 1–158.
661 Benning, L.G., and Waychunas, G.A. (2008) Nucleation, growth, and aggregation of mineral
662 phases: Mechanisms and kinetic controls. In S.L. Brantley, J.D. Kubicki, and A.F. White,
663 Eds., Kinetics of Water-Rock Interaction pp. 259–333. Springer, New York.
664 Benning, L.G., Wilkin, R.T., and Konhauser, K.O. (1999) Iron monosuphide stability:
665 Experiments with sulphate reducing bacteria. In H. Armannsson, Ed., Geochemistry of the
666 Earth's Surface pp. 429–432. A.A. Balkema, Rotterdam.
667 Benning, L.G., Wilkin, R.T., and Barnes, H.L. (2000) Reaction pathways in the Fe-S system
668 below 100^0C. Chemical Geology, 167, 25–51.
669 Berner, R.A. (1984) Sedimentary pyrite formation: An update. Geochimica et Cosmochimica
670 Acta, 48, 605–615.
671 Beveridge, T.J., and Koval, S.F. (1981) Binding of metals to cell envelopes of *Escherichia coli*
672 K-12. Apppied and Environmental Microbiology, 42, 325–335.
673 Beveridge, T.J., and Murray, R.G.E. (1976) Uptake and retention of metals by cell walls of
674 *Bacillus subtilis*. Journal of Bacteriology, 127, 1502–1518.
675 Boekema, C., Krupski, A.M., Varasteh, M., Parvin, K., Van Til, F., Van Der Woude, F., and
676 Sawatzky, G.A. (2004) Cu and Fe valence states in $CuFeS_2$. Journal of Magnetism and
677 Magnetic Materials, 272–276, 559–561.

678 Bosch, J., Lee, K.Y., Jordan, G., Kim, K.W., and Meckenstock, R.U. (2012) Anaerobic, nitrate-
679 dependent oxidation of pyrite nanoparticles by *Thiobacillus denitrificans*. Environmental
680 Science and Technology, 46, 2095–2101.
681 Bourdoiseau, J.A., Jeannin, M., Rémazeilles, C., Sabot, R., and Refait, P. (2011) The
682 transformation of mackinawite into greigite studied by Raman spectroscopy. Journal of
683 Raman Spectroscopy, 42, 496–504.
684 Burton, E.D., Bush, R.T., Sullivan, L.A., Hocking, R.K., Mitchell, D.R.G., Johnston, S.G.,
685 Fitzpatrick, R.W., Raven, M., McClure, S., and Jang, L.Y. (2009) Iron-monosulfide
686 oxidation in natural sediments: Resolving microbially mediated S transformations using
687 XANES, electron microscopy, and selective extractions. Environmental Science and
688 Technology, 43, 3128–3134.
689 Caraballo, M.A., Michel, F.M., and Hochella, M.F. (2015) The rapid expansion of environmental
690 mineralogy in unconventional ways: Beyond the accepted definition of a mineral, the latest
691 technology, and using nature as our guide. American Mineralogist, 100, 14–25.
692 Chen, G., Chen, X., Yang, Y., Hay, A.G., Yu, X., and Chen, Y. (2011) Sorption and distribution
693 of copper in unsaturated *Pseudomonas putida* CZ1 biofilms as determined by X-ray
694 fluorescence microscopy. Applied and Environmental Microbiology, 77, 4719–4727.
695 Ciglenečki, I., Krznarić, D., and Helz, G.R. (2005) Voltammetry of copper sulfide particles and
696 nanoparticles: Investigation of the cluster hypothesis. Environmental Science and
697 Technology, 39, 7492–7498.
698 Clark, A.H. (1971) A note on iron-bearing normal covellite. Neues Jahrbuch für Mineralogie:
699 Monatshefte, 424.
700 Conejeros, S., Alemany, P., Llunell, M., Moreira, I. de P.R., Sánchez, V., and Llanos, J. (2015)

Electronic structure and magnetic properties of $CuFeS_2$. Inorganic Chemistry, 54, 4840–4849.

Cowper, M., and Rickard, D. (1989) Mechanism of chalcopyrite formation from iron monosulphides in aqueous solutions (<100°C, pH 2-4.5). Chemical Geology, 78, 325–341.

Csákberényi-Malasics, D., Rodriguez-Blanco, J.D., Kis, V.K., Rečnik, A., Benning, L.G., and Pósfai, M. (2012) Structural properties and transformations of precipitated FeS. Chemical Geology, 294–295, 249–258.

da Costa, J.P., Girão, A.V., Lourenço, J.P., Monteiro, O.C., Trindade, T., and Costa, M.C. (2013) Green synthesis of covellite nanocrystals using biologically generated sulfide: Potential for bioremediation systems. Journal of Environmental Management, 128, 226–232.

De Los Ríos, A., Wierzchos, J., Sancho, L.G., and Ascaso, C. (2003) Acid microenvironments in microbial biofilms of antarctic endolithic microecosystems. Environmental Microbiology, 5, 231–237.

De Yoreo, J.J., Gilbert, P.U.P.A., Sommerdijk, N.A.J.M., Penn, R.L., Whitelam, S., Joester, D., Zhang, H., Rimer, J.D., Navrotsky, A., Banfield, J.F., and others (2015) Crystallization by particle attachment in synthetic, biogenic, and geologic environments. Science, 349, aaa6760.

Des Marais, D.J., Nuth, J.A., Allamandola, L.J., Boss, A.P., Farmer, J.D., Hoehler, T.M., Jakosky, B.M., Meadows, V.S., Pohorille, A., Runnegar, B., and others (2008) The NASA Astrobiology Roadmap. Astrobiology, 8, 715–730.

Donald, R., and Southam, G. (1999) Low temperature anaerobic bacterial diagenesis of ferrous monosulfide to pyrite. Geochimica et Cosmochimica Acta, 63, 2019–2023.

Downs, R.T., and Hall-Wallace, M. (2003) The *American Mineralogist* crystal structure

724 database. American Mineralogist, 88, 247–250.
725 Du, W., Qian, X., Xiaodong, M., Gong, Q., Cao, H., and Yin, J. (2007) Shape-controlled
726 synthesis and self-assembly of hexagonal covellite (CuS) nanoplatelets. Chemistry - A
727 European Journal, 13, 3241–3247.
728 Echigo, T., Aruguete, D.M., Murayama, M., and Hochella, M.F. (2012) Influence of size,
729 morphology, surface structure, and aggregation state on reductive dissolution of hematite
730 nanoparticles with ascorbic acid. Geochimica et Cosmochimica Acta, 90, 149–162.
731 Eskelsen, J.R., Xu, J., Chiu, M., Moon, J.W., Wilkins, B., Graham, D.E., Gu, B., and Pierce,
732 E.M. (2018) Influence of structural defects on biomineralized ZnS nanoparticle dissolution:
733 An in-situ electron microscopy study. Environmental Science and Technology, 52, 1139–
734 1149.
735 Falagán, C., Grail, B.M., and Johnson, D.B. (2017) New approaches for extracting and
736 recovering metals from mine tailings. Minerals Engineering, 106, 71–78.
737 Ferris, F., Schultze, S., Witten, T., Fyfe, W., Beveridge, T., and Schultz, S. (1989) Metal
738 interactions with microbial biofilms in acidic and neutral pH environments. Applied and
739 Environmental Microbiology, 55, 1249–1257.
740 Fortin, D., Southam, G., and Beveridge, T.J. (1994) Nickel sulfide, iron-nickel sulfide and iron
741 sulfide precipitation by a newly isolated *Desulfotomaculum* species and its relation to nickel
742 resistance. FEMS Microbiology Ecology, 14, 121–132.
743 Fulda, B., Voegelin, A., Ehlert, K., and Kretzschmar, R. (2013) Redox transformation, solid
744 phase speciation and solution dynamics of copper during soil reduction and reoxidation as
745 affected by sulfate availability. Geochimica et Cosmochimica Acta, 123, 385–402.
746 Gartman, A., Findlay, A.J., and Luther, G.W. (2014) Nanoparticulate pyrite and other

747 nanoparticles are a widespread component of hydrothermal vent black smoker emissions.
748 Chemical Geology, 366, 32–41.
749 Goh, S.W., Buckley, A.N., Lamb, R.N., Rosenberg, R.A., and Moran, D. (2006) The oxidation
750 states of copper and iron in mineral sulfides, and the oxides formed on initial exposure of
751 chalcopyrite and bornite to air. Geochimica et Cosmochimica Acta, 70, 2210–2228.
752 Gramp, J.P., Sasaki, K., Bigham, J.M., Karnachuk, O. V., and Tuovinen, O.H. (2006) Formation
753 of covellite (CuS) under biological sulfate-reducing conditions. Geomicrobiology Journal,
754 23, 613–619.
755 Gramp, J.P., Bigham, J.M., Jones, F.S., and Tuovinen, O.H. (2010) Formation of Fe-sulfides in
756 cultures of sulfate-reducing bacteria. Journal of Hazardous Materials, 175, 1062–1067.
757 Gregory, D.D., Large, R.R., Halpin, J.A., Baturina, E.L., Lyons, T.W., Wu, S., Danyushevsky,
758 L., Sack, P.J., Chappaz, A., Maslennikov, V. V, and others (2015) Trace element content of
759 sedimentary pyrite in black shales. Economic Geology, 110, 1389–1410.
760 Guilbaud, R., Butler, I.B., Ellam, R.M., and Rickard, D. (2010) Fe isotope exchange between
761 $Fe(II)_{aq}$ and nanoparticulate mackinawite (FeS_m) during nanoparticle growth. Earth and
762 Planetary Science Letters, 300, 174–183.
763 Hao, L., Li, J., Kappler, A., and Obst, M. (2013) Mapping of heavy metal ion sorption to cell-
764 extracellular polymeric substance-mineral aggregates by using metal-selective fluorescent
765 probes and confocal laser scanning microscopy. Applied and Environmental Microbiology,
766 79, 6524–6534.
767 Harmandas, N.G., and Koutsoukos, P.G. (1996) The formation of iron(II) sulfides in aqueous
768 solutions. Journal of Crystal Growth, 167, 719–724.
769 Harmandas, N.G., Navarro Fernandez, E., and Koutsoukos, P.G. (1998) Crystal growth of pyrite

770 in aqueous solutions. Inhibition by organophosphorus compounds. Langmuir, 14, 1250–
771 1255.
772 Heidelberg, J.F., Seshadri, R., Haveman, S.A., Hemme, C.L., Paulsen, I.T., Kolonay, J.F., Eisen,
773 J.A., Ward, N., Methe, B., Brinkac, L.M., and others (2004) The genome sequence of the
774 anaerobic, sulfate-reducing bacterium *Desulfovibrio vulgaris* Hildenborough. Nature
775 Biotechnology, 22, 554–559.
776 Herbert, R.B., Benner, S.G., Pratt, A.R., and Blowes, D.W. (1998) Surface chemistry and
777 morphology of poorly crystalline iron sulfides precipitated in media containing sulfate-
778 reducing bacteria. Chemical Geology, 144, 87–97.
779 Hidalgo, G., Burns, A., Herz, E., Hay, A.G., Houston, P.L., Wiesner, U., and Lion, L.W. (2009)
780 Functional tomographic fluorescence imaging of pH microenvironments in microbial
781 biofilms by use of silica nanoparticle sensors. Applied and Environmental Microbiology,
782 75, 7426–7435.
783 Hochella, M.F., Moore, J.N., Putnis, C. V., Putnis, A., Kasama, T., and Eberl, D.D. (2005) Direct
784 observation of heavy metal-mineral association from the Clark Fork River Superfund
785 Complex: Implications for metal transport and bioavailability. Geochimica et
786 Cosmochimica Acta, 69, 1651–1663.
787 Hochella, M.F., Lower, S.K., Maurice, P.A., Penn, R.L., Sahai, N., Sparks, D.L., and Twining,
788 B.S. (2008) Nanominerals, mineral nanoparticles, and Earth systems. Science, 319, 1631–
789 1635.
790 Hochella, M.F., Aruguete, D.M., Kim, B., and Madden, A.S. (2012) Naturally occurring
791 inorganic nanoparticles: General assessment and a global budget for one of Earth's last
792 unexplored geochemical components. In A.S. Barnard and H. Guo, Eds., Nature' s

793 Nanostructures pp. 1–42. Pan Stanford Publishing, Singapore.
794 Hofacker, A.F., Voegelin, A., Kaegi, R., Weber, F.A., and Kretzschmar, R. (2013) Temperature-
795 dependent formation of metallic copper and metal sulfide nanoparticles during flooding of a
796 contaminated soil. Geochimica et Cosmochimica Acta, 103, 316–332.
797 Horneck, G., Walter, N., Westall, F., Grenfell, J.L., Martin, W.F., Gomez, F., Leuko, S., Lee, N.,
798 Onofri, S., Tsiganis, K., and others (2016) AstRoMap European Astrobiology Roadmap.
799 Astrobiology, 16, 201–243.
800 Hunter, R.C., and Beveridge, T.J. (2005) Application of a pH-sensitive gluoroprobe (C-SNARF-
801 4) for pH microenvironment analysis in *Pseudomonas aeruginosa* biofilms. Applied and
802 Environmental Microbiology, 71, 2501–2510.
803 Ikkert, O.P., Gerasimchuk, A.L., Bukhtiyarova, P.A., Tuovinen, O.H., and Karnachuk, O. V.
804 (2013) Characterization of precipitates formed by H_2S-producing, Cu-resistant *Firmicute*
805 isolates of *Tissierella* from human gut and *Desulfosporosinus* from mine waste. Antonie
806 van Leeuwenhoek, International Journal of General and Molecular Microbiology, 103,
807 1221–1234.
808 Ikogou, M., Ona-Nguema, G., Juillot, F., Le Pape, P., Menguy, N., Richeux, N., Guigner, J.M.,
809 Noël, V., Brest, J., Baptiste, B., and others (2017) Long-term sequestration of nickel in
810 mackinawite formed by *Desulfovibrio capillatus* upon Fe(III)-citrate reduction in the
811 presence of thiosulfate. Applied Geochemistry, 80, 143–154.
812 Ikuma, K., Decho, A.W., and Lau, B.L.T. (2015) When nanoparticles meet biofilms -
813 Interactions guiding the environmental fate and accumulation of nanoparticles. Frontiers in
814 Microbiology, 6, 1–6.
815 Jalali, K.K., and Baldwin, S.A. (2000) The role of sulfate reducing bacteria in copper removal

816 from aqueous sulfate solutions. Water Research, 34, 797–806.
817 Karnachuk, O. V., Sasaki, K., Gerasimchuk, A.L., Sukhanova, O., Ivasenko, D.A., Kaksonen,
818 A.H., Puhakka, J.A., and Tuovinen, O.H. (2008) Precipitation of Cu-sulfides by copper-
819 tolerant *Desulfovibrio* isolates. Geomicrobiology Journal, 25, 219–227.
820 Kiran, M.G., Pakshirajan, K., and Das, G. (2015) Heavy metal removal using sulfate-reducing
821 biomass obtained from a lab-scale upflow anaerobic-packed bed reactor. Environmental
822 Engineering, 142, 1–8.
823 Klekovkina, V. V., Gainov, R.R., Vagizov, F.G., Dooglav, A. V., Golovanevskiy, V.A., and
824 Pen'kov, I.N. (2014) Oxidation and magnetic states of chalcopyrite $CuFeS_2$: A first
825 principles calculation. Optics and Spectroscopy, 116, 885–888.
826 Kwon, K.D., Refson, K., and Sposito, G. (2015) Transition metal incorporation into mackinawite
827 (tetragonal FeS). American Mineralogist, 100, 1509–1517.
828 Labrenz, M., Druschel, G.K., Thomsen-Ebert, T., Gilbert, B., Welch, S.A., Kemner, K.M.,
829 Logan, G.A., Summons, R.E., De Stasio, G., Bond, P.L., and others (2000) Formation of
830 sphalerite (ZnS) deposits in natural biofilms of sulfate-reducing bacteria. Science, 290,
831 1744–1747.
832 Langford, J.I., and Wilson, A.J.C. (1978) Scherrer after sixty years: A survey and some new
833 results in the determination of crystallite size. Journal of Applied Crystallography, 11, 102–
834 113.
835 Large, R.R., Halpin, J.A., Danyushevsky, L. V., Maslennikov, V. V., Bull, S.W., Long, J.A.,
836 Gregory, D.D., Lounejeva, E., Lyons, T.W., Sack, P.J., and others (2014) Trace element
837 content of sedimentary pyrite as a new proxy for deep-time ocean-atmosphere evolution.
838 Earth and Planetary Science Letters, 389, 209–220.

839 Lead, J.R., and Wilkinson, K.J. (2006) Aquatic colloids and nanoparticles: Current knowledge
840 and future trends. Environmental Chemistry, 3, 159–171.
841 Lennie, A.R. (1995) Synthesis and Rietveld crystal structure refinement of mackinawite,
842 tetragonal FeS. Mineralogical Magazine, 59, 677–683.
843 Lett, R.E.W., and Fletcher, W.K. (1980) Syngenetic sulphide minerals in a copper-rich bog.
844 Mineralium Deposita, 15, 61–67.
845 Li, W., Shavel, A., Guzman, R., Rubio-Garcia, J., Flox, C., Fan, J., Cadavid, D., Ibáñez, M.,
846 Arbiol, J., Morante, J.R., and others (2011) Morphology evolution of $Cu_{2-x}S$ nanoparticles:
847 from spheres to dodecahedrons. Chemical Communications, 47, 10332.
848 Liang, Y.J., Chai, L.Y., Min, X.B., Tang, C.J., Zhang, H.J., Ke, Y., and Xie, X. De (2012)
849 Hydrothermal sulfidation and floatation treatment of heavy-metal-containing sludge for
850 recovery and stabilization. Journal of Hazardous Materials, 217–218, 307–314.
851 Libert, S., Gorshkov, V., Privman, V., Goia, D., and Matijević, E. (2003) Formation of
852 monodispersed cadmium sulfide particles by aggregation of nanosize precursors. Advances
853 in Colloid and Interface Science, 100–102, 169–183.
854 Liu, Y., Yin, D., and Swihart, M.T. (2018) Valence selectivity of cation incorporation into
855 covellite CuS nanoplatelets. Chemistry of Materials, 30, 1399–1407.
856 Luther, G.W. (1991) Pyrite synthesis via polysulfide compounds. Geochimica et Cosmochimica
857 Acta, 55, 2839–2849.
858 Luther, G.W., and Rickard, D.T. (2005) Metal sulfide cluster complexes and their
859 biogeochemical importance in the environment. Journal of Nanoparticle Research, 7, 389–
860 407.
861 Luther, G.W., Theberge, S.M., Rozan, T.F., Rickard, D., Rowlands, C.C., and Oldroyd, A.

(2002) Aqueous copper sulfide clusters as intermediates during copper sulfide formation. Environmental Science and Technology, 36, 394–402.

Mansor, M., Hamilton, T.L., Fantle, M.S., and Macalady, J.L. (2015) Metabolic diversity and ecological niches of *Achromatium* populations revealed with single-cell genomic sequencing. Frontiers in Microbiology, 6, 1–14.

Mantha, H., Schindler, M., and Hochella, M.F. (2019) Occurrence and formation of incidental metallic Cu and CuS nanoparticles in organic-rich contaminated surface soils in Timmins, Ontario. In press. Environmental Science: Nano.

Maydagán, L., Franchini, M., Lentz, D., Pons, J., and McFarlane, C. (2013) Sulfide composition and isotopic signature of the Altar Cu-Au deposit: Argentina: Constraints on the evolution of the porphyry-epithermal system. The Canadian Mineralogist, 51, 813–840.

Melekestseva, I.Y., Maslennikov, V. V., Maslennikova, S.P., Danyushevsky, L. V., and Large, R. (2017) Covellite of the Semenov-2 hydrothermal field (13°31.13′ N, Mid-Atlantic Ridge): Enrichment in trace elements according to LA ICP MS analysis. Doklady Earth Sciences, 473, 291–295.

Michel, F.M., Antao, S.M., Chupas, P.J., Lee, P.L., Parise, J.B., and Schoonen, M.A.A. (2005) Short- to medium-range atomic order and crystallite size of the initial FeS precipitate from pair distribution function analysis. Chemistry of Materials, 17, 6246–6255.

Morales-García, Á., He, J., Soares, A.L., and Duarte, H.A. (2017) Surfaces and morphologies of covellite (CuS) nanoparticles by means of: Ab initio atomistic thermodynamics. CrystEngComm, 19, 3078–3084.

Moreau, J.W., Webb, R.I., and Banfield, J.F. (2004) Ultrastructure, aggregation-state, and crystal growth of biogenic nanocrystalline sphalerite and wurtzite. American Mineralogist, 89,

950–960.

Moreau, J.W., Weber, P.K., Martin, M.C., Gilbert, B., Hutcheon, I.D., and Banfield, J.F. (2007) Extracellular proteins limit the dispersal of biogenic nanoparticles. Science, 316, 13–16.

Morin, G., Noël, V., Menguy, N., Brest, J., Baptiste, B., Tharaud, M., Ona-Nguema, G., Ikogou, M., Viollier, E., and Juillot, F. (2017) Nickel accelerates pyrite nucleation at ambient temperature. Geochemical Perspectives Letters, 6–11.

Morse, J.W., and Arakaki, T. (1993) Adsorption and coprecipitation of divalent metals with mackinawite (FeS). Geochimica et Cosmochimica Acta, 57, 3635–3640.

Morse, J.W., and Luther, G.W. (1999) Chemical influence on trace metal-sulfide interactions in anoxic sediments. Geochimica et Cosmochimica Acta, 63, 3378.

Mullaugh, K.M., and Luther, G.W. (2011) Growth kinetics and long-term stability of CdS nanoparticles in aqueous solution under ambient conditions. Journal of Nanoparticle Research, 13, 393–404.

Newbury, D.E., and Ritchie, N.W.M. (2014) Performing elemental microanalysis with high accuracy and high precision by scanning electron microscopy/silicon drift detector energy-dispersive X-ray spectrometry (SEM/SDD-EDS). Journal of Materials Science, 50, 493–518.

Niu, Z., Pan, H., Guo, X., Lu, D., Feng, J., Chen, Y., Tou, F., Liu, M., and Yang, Y. (2018) Sulphate-reducing bacteria (SRB) in the Yangtze Estuary sediments: Abundance, distribution and implications for the bioavailibility of metals. Science of the Total Environment, 634, 296–304.

Nowack, B., Ranville, J.F., Diamond, S., Gallego-Urrea, J.A., Metcalfe, C., Rose, J., Horne, N., Koelmans, A.A., and Klaine, S.J. (2012) Potential scenarios for nanomaterial release and

908 subsequent alteration in the environment. Environmental Toxicology and Chemistry, 31,
909 50–59.
910 Ohfuji, H., and Rickard, D. (2006) High resolution transmission electron microscopic study of
911 synthetic nanocrystalline mackinawite. Earth and Planetary Science Letters, 241, 227–233.
912 Pankhania, I.P., Gow, L.A., and Hamilton, W.A. (1986) The effect of hydrogen on the growth of
913 *Desulfovibrio vulgaris* (Hildenborough) on lactate. Journal of General Microbiology, 132,
914 3349–3356.
915 Parkman, R.H., Charnock, J.M., Bryan, N.D., Livens, F.R., and Vaughan, D.J. (1999) Reactions
916 of copper and cadmium ions in aqueous solution with goethite, lepidocrocite, mackinawite,
917 and pyrite. American Mineralogist, 84, 407–419.
918 Pattrick, R.A.D., Mosselmans, J.F.W., Charnock, J.M., England, K.E.R., Helz, G.R., Garner,
919 C.D., and Vaughan, D.J. (1997) The structure of amorphous copper sulfide precipitates: An
920 X-ray absorption study. Geochimica et Cosmochimica Acta, 61, 2023–2036.
921 Pearce, C.I., Pattrick, R.A.D., Vaughan, D.J., Henderson, C.M.B., and van der Laan, G. (2006)
922 Copper oxidation state in chalcopyrite: Mixed Cu d^9 and d^{10} characteristics. Geochimica et
923 Cosmochimica Acta, 70, 4635–4642.
924 Penn, R.L., and Banfield, J.F. (1998) Imperfect oriented attachment: dislocation generation in
925 defect-free nanocrystals. Science, 281, 969–971.
926 Picard, A., Gartman, A., and Girguis, P.R. (2016) What do we really know about the role of
927 microorganisms in iron sulfide mineral formation? Frontiers in Earth Science, 4, 1–10.
928 Picard, A., Gartman, A., Clarke, D.R., and Girguis, P.R. (2018) Sulfate-reducing bacteria
929 influence the nucleation and growth of mackinawite and greigite. Geochimica et
930 Cosmochimica Acta, 220, 367–384.

Pileni, M.P., Motte, L., Billoudet, F., Mahrt, J., and Willig, F. (1997) Nanosized silver sulfide particles: characterization, self-organization into 2D and 3D superlattices. Materials Letters, 31, 255–260.

Qafoku, N.P., Gartman, B.N., Kukkadapu, R.K., Arey, B.W., Williams, K.H., Mouser, P.J., Heald, S.M., Bargar, J.R., Janot, N., Yabusaki, S., and others (2014) Geochemical and mineralogical investigation of uranium in multi-element contaminated, organic-rich subsurface sediment. Applied Geochemistry, 42, 77–85.

Rice, C.M., Atkin, D., Bowles, J.F.W., and Criddle, A.J. (1979) Nukundamite, a new mineral, and idaite. Mineralogical Magazine, 43, 193–200.

Rickard, D. (1975) Kinetics and mechanism of pyrite formation at low temperatures. American Journal of Science, 275, 636–652.

Rickard, D., and Luther, G.W. (2006) Metal sulfide complexes and clusters. Reviews in Mineralogy and Geochemistry, 61, 421–504.

Rickard, D., and Luther, G.W. (2007) Chemistry of iron sulfides. Chemical Reviews, 107, 514–562.

Roberts, W.M.B. (1961) Formation of chalcopyrite by reaction between chalcocite and pyrrhotite in cold solution. Nature, 191, 560–562.

Roberts, W.M.B. (1963) The low temperature synthesis in aqueous solution of chalcopyrite and bornite. Economic Geology, 58, 52–61.

Sampaio, R.M.M., Timmers, R.A., Xu, Y., Keesman, K.J., and Lens, P.N.L. (2009) Selective precipitation of Cu from Zn in a pS controlled continuously stirred tank reactor. Journal of Hazardous Materials, 165, 256–265.

Schliehe, C., Juarez, B.H., Pelletier, M., Jander, S., Greshnykh, D., Nagel, M., Meyer, A.,

954 Foerster, S., Kornowski, A., Klinke, C., and others (2010) Ultrathin PbS sheets by two-
955 dimensional oriented attachment. Science, 74, 550–554.
956 Schoonen, M.A., and Barnes, H.L. (1991) Reactions forming pyrite and marcasite from solution:
957 II. Via FeS precursors below 100°C. Geochimica et Cosmochimica Acta, 55, 1505–1514.
958 Sharma, V.K., Filip, J., Zboril, R., and Varma, R.S. (2015) Natural inorganic nanoparticles –
959 formation, fate, and toxicity in the environment. Chemical Society Reviews, 44, 8410–
960 8423.
961 Shea, D., and Helz, G.R. (1989) Solubility product constants of covellite and a poorly crystalline
962 copper sulfide precipitate at 298 K. Geochimica et Cosmochimica Acta, 53, 229–236.
963 Sitte, J., Pollok, K., Langenhorst, F., and Küsel, K. (2013) Nanocrystalline nickel and cobalt
964 sulfides formed by a heavy metal-tolerant, sulfate-reducing enrichment culture.
965 Geomicrobiology Journal, 30, 36–47.
966 Sugaki, A., Shima, H., Kitakaze, A., and Mizota, T. (1981) Hydrothermal synthesis of
967 nukundamite and its crystal structure. American Mineralogist, 66, 398–402.
968 Triboulet, S., Aude-Garcia, C., Armand, L., Collin-Faure, V., Chevallet, M., Diemer, H., Gerdil,
969 A., Proamer, F., Strub, J.M., Habert, A., and others (2015) Comparative proteomic analysis
970 of the molecular responses of mouse macrophages to titanium dioxide and copper oxide
971 nanoparticles unravels some toxic mechanisms for copper oxide nanoparticles in
972 macrophages. PLoS ONE, 10, 1–22.
973 Veeramani, H., Scheinost, A.C., Monsegue, N., Qafoku, N.P., Kukkadapu, R., Newville, M.,
974 Lanzirotti, A., Pruden, A., Murayama, M., and Hochella, M.F. (2013) Abiotic reductive
975 immobilization of U(VI) by biogenic mackinawite. Environmental Science and Technology,
976 47, 2361–2369.

977 Voordouw, G. (2002) Carbon monoxide cycling by *Desulfovibrio vulgaris* Hildenborough.
978 Journal of Bacteriology, 184, 5903–5911.
979 Wan, M., Schröder, C., and Peiffer, S. (2017) Fe(III):S(-II) concentration ratio controls the
980 pathway and the kinetics of pyrite formation during sulfidation of ferric hydroxides.
981 Geochimica et Cosmochimica Acta.
982 Weber, F.A., Voegelin, A., Kaegi, R., and Kretzschmar, R. (2009a) Contaminant mobilization by
983 metallic copper and metal sulphide colloids in flooded soil. Nature Geoscience, 2, 267–271.
984 Weber, F.A., Voegelin, A., and Kretzschmar, R. (2009b) Multi-metal contaminant dynamics in
985 temporarily flooded soil under sulfate limitation. Geochimica et Cosmochimica Acta, 73,
986 5513–5527.
987 White, L.M., Bhartia, R., Stucky, G.D., Kanik, I., and Russell, M.J. (2015) Mackinawite and
988 greigite in ancient alkaline hydrothermal chimneys: Identifying potential key catalysts for
989 emergent life. Earth and Planetary Science Letters, 430, 105–114.
990 Wilkin, R.T., and Beak, D.G. (2017) Uptake of nickel by synthetic mackinawite. Chemical
991 Geology, 462, 15–29.
992 Wolthers, M., Van der Gaast, S.J., and Rickard, D. (2003) The structure of disordered
993 mackinawite. American Mineralogist, 88, 2007–2015.
994 Xu, H.L., Wang, W.Z., and Zhu, W. (2006) Oriented attachment of crystalline CuS nanorods.
995 Chemistry Letters, 35, 264–265.
996 Xu, J., Murayama, M., Roco, C.M., Veeramani, H., Michel, F.M., Rimstidt, J.D., Winkler, C.,
997 and Hochella, M.F. (2016) Highly-defective nanocrystals of ZnS formed via dissimilatory
998 bacterial sulfate reduction: A comparative study with their abiogenic analogues.
999 Geochimica et Cosmochimica Acta, 180, 1–14.

Xu, J., Veeramani, H., Qafoku, N.P., Singh, G., Riquelme, M. V, Pruden, A., Kukkadapu, R.K., Gartman, B.N., and Hochella, M.F. (2017) Efficacy of acetate-amended biostimulation for uranium sequestration: Combined analysis of sediment / groundwater geochemistry and bacterial community structure. Applied Geochemistry, 78, 172–185.

Yücel, M., Gartman, A., Chan, C.S., and Luther, G.W. (2011) Hydrothermal vents as a kinetically stable source of iron-sulphide-bearing nanoparticles to the ocean. Nature Geoscience, 4, 367–371.

Zavašnik, J., Stanković, N., Arshad, S.M., and Rečnik, A. (2014) Sonochemical synthesis of mackinawite and the role of Cu addition on phase transformations in the Fe-S system. Journal of Nanoparticle Research, 16.

Zbinden, M., Martinez, I., Guyot, F., Cambon-Bonavita, M.-A., and Gaill, F. (2001) Zinc-iron sulphide mineralization in tubes of hydrothermal vent worms. European Journal of Mineralogy, 13, 653–658.

Zhang, H., Zhang, Y., Yu, J., and Yang, D. (2008) Phase-selective synthesis and self-assembly of monodisperse copper sulfide nanocrystals. Journal of Physical Chemistry C, 112, 13390–13394.

Zhou, C., Vannela, R., Hayes, K.F., and Rittmann, B.E. (2014) Effect of growth conditions on microbial activity and iron-sulfide production by *Desulfovibrio vulgaris*. Journal of Hazardous Materials, 272, 28–35.

This is a preprint, the final version is subject to change, of the American Mineralogist (MSA)
Cite as Authors (Year) Title. American Mineralogist, in press.
DOI: https://doi.org/10.2138/am-2019-6848

1023 **Tables**

1024 **Table 1**: XRD-derived parameters for the (001) plane of mackinawite. Samples from this study
1025 were measured at least in duplicates.

System	d-spacing (Å)		Size (nm)	
	Biogenic	Abiogenic	Biogenic	Abiogenic
1:0 Fe:Cu	4.91 to 5.09	4.94 to 5.02	7 to 9	4 to 6
1:0 Fe:Cu*	5.04 to 5.07	4.98 to 5.24	9 to 26	3 to 9
2:1 Fe:Cu	4.72 to 4.73	5.10 to 5.17	≤ 3	≤ 3
1:1 Fe:Cu	-	5.25 to 5.32	-	≤ 3

1026 *Fe only experiments from Picard et al. (2018). Biogenic mackinawite data from experiments containing
1027 microbes (live or dead) and abiogenic mackinawite data from experiments performed in the absence of
1028 microbes.

1029

1030

1031

1032

1033

1034

1035

1036

1037

1038

1039 **Table 2**: Compiled d-spacing values (in Å) and corresponding planes for selected minerals based
1040 on the American Mineralogist Crystal Structure Database
1041 (http://rruff.geo.arizona.edu/AMS/amcsd.php; accessed date January 9, 2019; Downs and Hall-
1042 Wallace, 2003). Bolded values indicate major diffraction peaks, defined as having a relative
1043 intensity > 0.2 compared to the most intense peak when analyzed by XRD.

d-spacing (hkl)				
Mackinawite	Greigite	Covellite	Chalcopyrite	Nukundamite
5.03 (001)	5.70 (111)	8.18 (002)	3.04 (112)	11.20 (001)
2.97 (101)	3.49 (220)	4.09 (004)	2.64 (200)	5.60 (002)
2.56 (110)	2.98 (311)	3.29 (100)	2.61 (004)	3.73 (003)
2.52 (002)	2.47 (400)	3.22 (101)	1.87 (220)	3.28 (100)
2.31 (111)	2.27 (331)	3.05 (102)	1.86 (204)	3.14 (101)
1.84 (200)	2.02 (422)	2.82 (103)	1.59 (312)	2.83 (012)
1.81 (112)	1.90 (511)	2.73 (006)	1.58 (116)	2.83 (102)
1.73 (201)	1.90 (333)	2.32 (105)		2.80 (004)
1.68 (003)	1.75 (440)	2.10 (106)		2.46 (013)
1.56 (211)	1.56 (620)	2.05 (008)		2.24 (005)
		1.90 (107)		2.13 (104)
		1.898 (110)		1.89 (110)
		1.74 (108)		1.85 (015)
		1.65 (200)		1.85 (105)
		1.64 (201)		1.79 (112)
		1.62 (202)		1.68 (113)
		1.59 (109)		1.64 (200)
		1.57 (203)		1.62 (016)
		1.56 (116)		1.62 (106)
				1.62 (021)
				1.60 (007)
				1.57 (022)
				1.57 (202)
				1.567 (114)

1044

1045

1046

1047 **Figure Captions**

1048 **Figure 1**: XRD patterns of biogenic (*Bio*) and abiogenic (*Abio*) precipitates, with different panels
1049 corresponding to the initial aqueous Fe-to-Cu ratios. Reference patterns of relevant phases are
1050 shown at the bottom of each panel.

1051 **Figure 2**: TEM images of nanoparticles precipitated at different initial aqueous Fe-to-Cu ratios
1052 as arranged by row. The final column shows representative wide-view (>50 nm spot size) SAED
1053 patterns for the samples, with d-spacings that are consistent with (from top to bottom row)
1054 mackinawite, covellite, covellite, chalcopyrite and chalcopyrite. (a-d) Wrinkled nanosheet
1055 composed of mackinawite aggregates, with electron-dense regions exhibiting fibrous-like
1056 structures. (e-h) From left to right: <10 nm fine covellite nanocrystals, nanorods and nanoplates.
1057 The SAED pattern is collected from aggregates containing all three morphologies. (i-l) Images
1058 focusing on Fe-rich euhedral covellite nanoparticles. The SAED pattern is collected from a
1059 single euhedral crystal (distinct diffraction spots) that is surrounded by fine covellite
1060 nanocrystals (diffraction rings). (m-p) Chalcopyrite aggregates composed primarily of <10 nm
1061 fine nanocrystals, with corresponding diffraction rings in the SAED pattern. In the same sample,
1062 minor amounts of nanorods and nanoplates (with variable Fe/(Fe+Cu) ratios) are also visible
1063 (panel o). (q-t) Chalcopyrite aggregates composed primarily of <10 nm fine nanocrystals, with
1064 corresponding diffraction rings in the SAED pattern.

1065 **Figure 3**: TEM images focusing on the different nanoparticle morphology. (a-b) Greigite
1066 nanoplates with corresponding SAED pattern derived from multiple greigite crystals. (c-d)
1067 Greigite-mackinawite aggregates with corresponding SAED patterns. The 5.78 Å d-spacing is
1068 characteristic of greigite (111) reflection, while the rest of the diffraction rings can be attributed
1069 to either greigite or mackinawite (e-h) Covellite nanorods with predominantly (102) or (103)

plane perpendicular to the direction of elongation. Defects within the crystal structures (electron dense regions or kinks) are highlighted in yellow boxes. (i-l) Covellite nanoplates with poorly-defined edges. Insets show either the whole-area SAED (panel i and j) or FFT-derived diffraction patterns from partial areas defined by the black square outline (panel k and l). Note that the diffraction patterns may reflect multiple overlapping crystals. (m-p) Euhedral nanoparticles of Fe-rich covellite. These NPs are larger and thicker compared to the thin nanoplates in panel i-l. (q-t) Large tabular NPs and nanoparticle aggregates in mixed metal Fe-Cu systems ($M_{Fe/Cu}$ = 1:5 and 1:1). The SAED patterns display d-spacing values of ~3.15 Å, consistent with the (101) reflection of nukundamite ($Cu_{5.5}Fe_{6.5}$). Other d-spacing values are ambiguous and can be assigned either to covellite, chalcopyrite or nukundamite.

Figure 4: EDS maps of (a) euhedral Fe-rich covellite crystals precipitated at 1:5 Fe:Cu ratio, displaying fairly homogenous Fe distribution within their structures and (b) aggregates of chalcopyrite precipitated at 1:1 Fe:Cu ratio.

Figure 5: Size dimensions for (a-b) nanorods and (c) nanoplates. Numbers in the bar charts indicate the number of crystals that was measured from TEM images.

Figure 6: A pseudo-nanorod structure that is composed of oriented arrangement of smaller covellite nanocrystals (inset). Within the structure, smaller areas that show more coherent arrangements are highlighted in yellow.

Figure 7: High-resolution images of fine covellite nanocrystals and nanorods, focusing on defects within the crystal structure as outlined in yellow. Boundaries of the fine nanocrystals are outlined in black to assist visualization. (a) Twinning and (b-c) stacking faults can be observed within < 10 nm nanocrystals across the (100)/(101) or (102) planes. (d-e) Stacking faults and

1092 kinks can be observed within nanorods. The morphological variety of fine covellite nanocrystals
1093 with different planes exposed are also evident.

This is a preprint, the final version is subject to change, of the American Mineralogist (MSA)
Cite as Authors (Year) Title. American Mineralogist, in press.
DOI: https://doi.org/10.2138/am-2019-6848

Figure 1

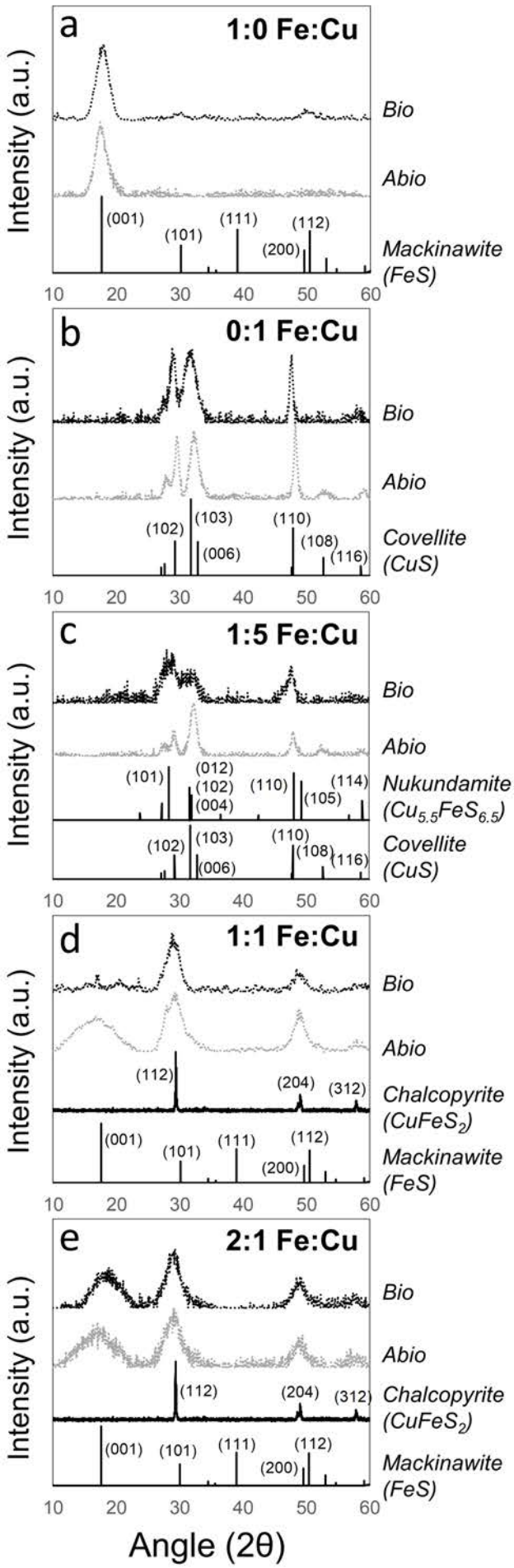

This is a preprint, the final version is subject to change, of the American Mineralogist (MSA)
Cite as Authors (Year) Title. American Mineralogist, in press.
DOI: https://doi.org/10.2138/am-2019-6848

Figure 2

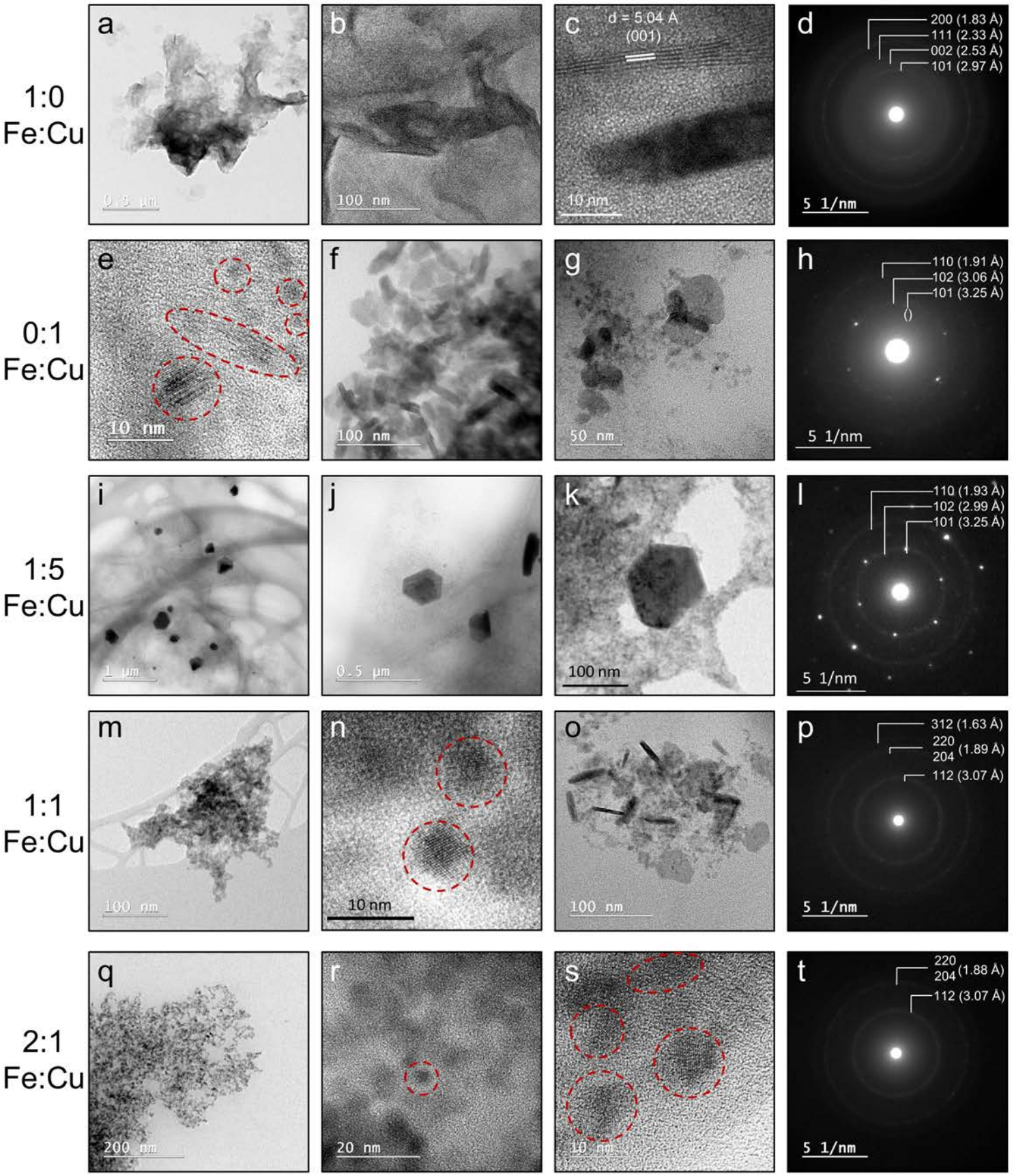

This is a preprint, the final version is subject to change, of the American Mineralogist (MSA)
Cite as Authors (Year) Title. American Mineralogist, in press.
DOI: https://doi.org/10.2138/am-2019-6848

Figure 3

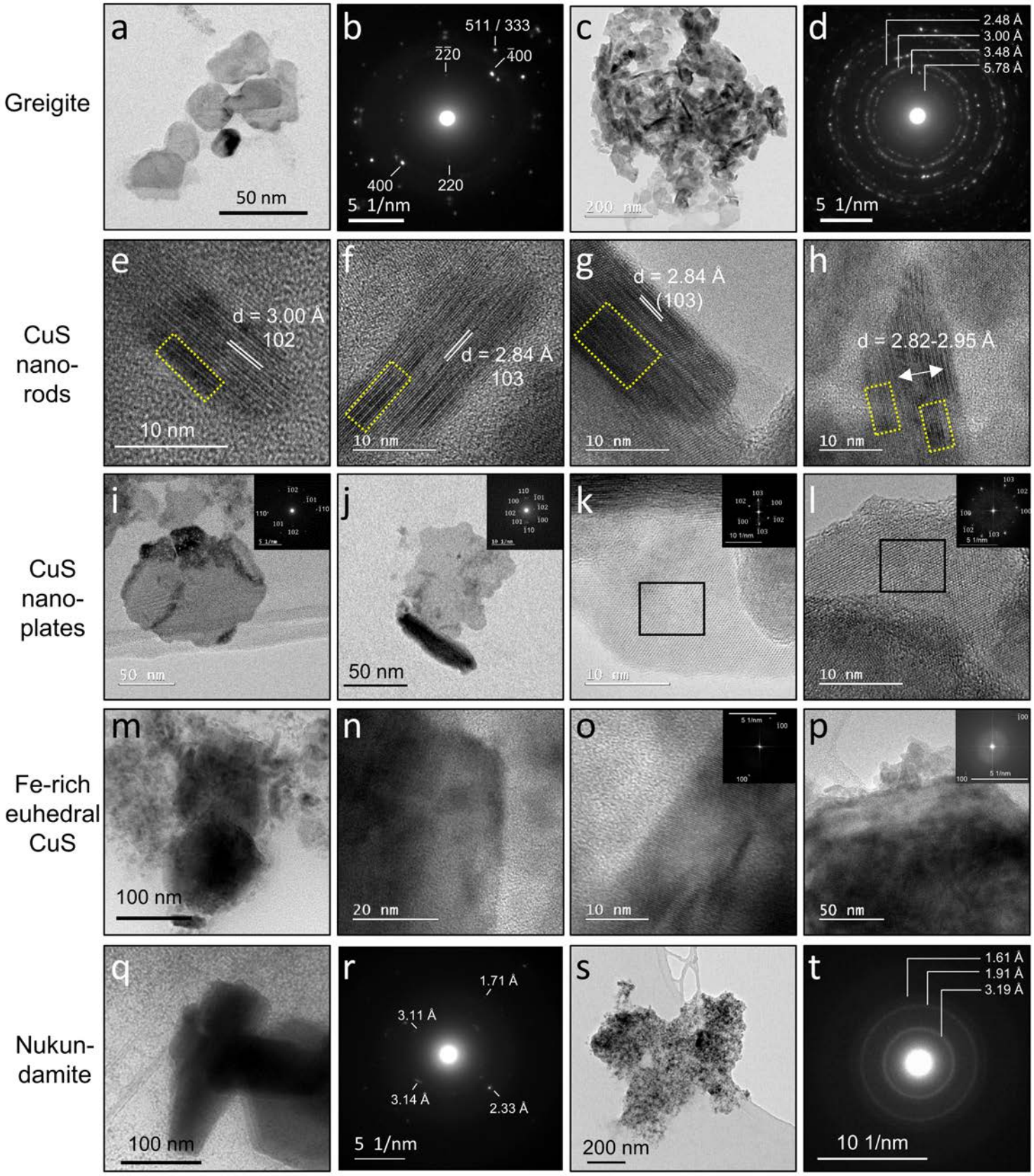

This is a preprint, the final version is subject to change, of the American Mineralogist (MSA)
Cite as Authors (Year) Title. American Mineralogist, in press.
DOI: https://doi.org/10.2138/am-2019-6848

Figure 4

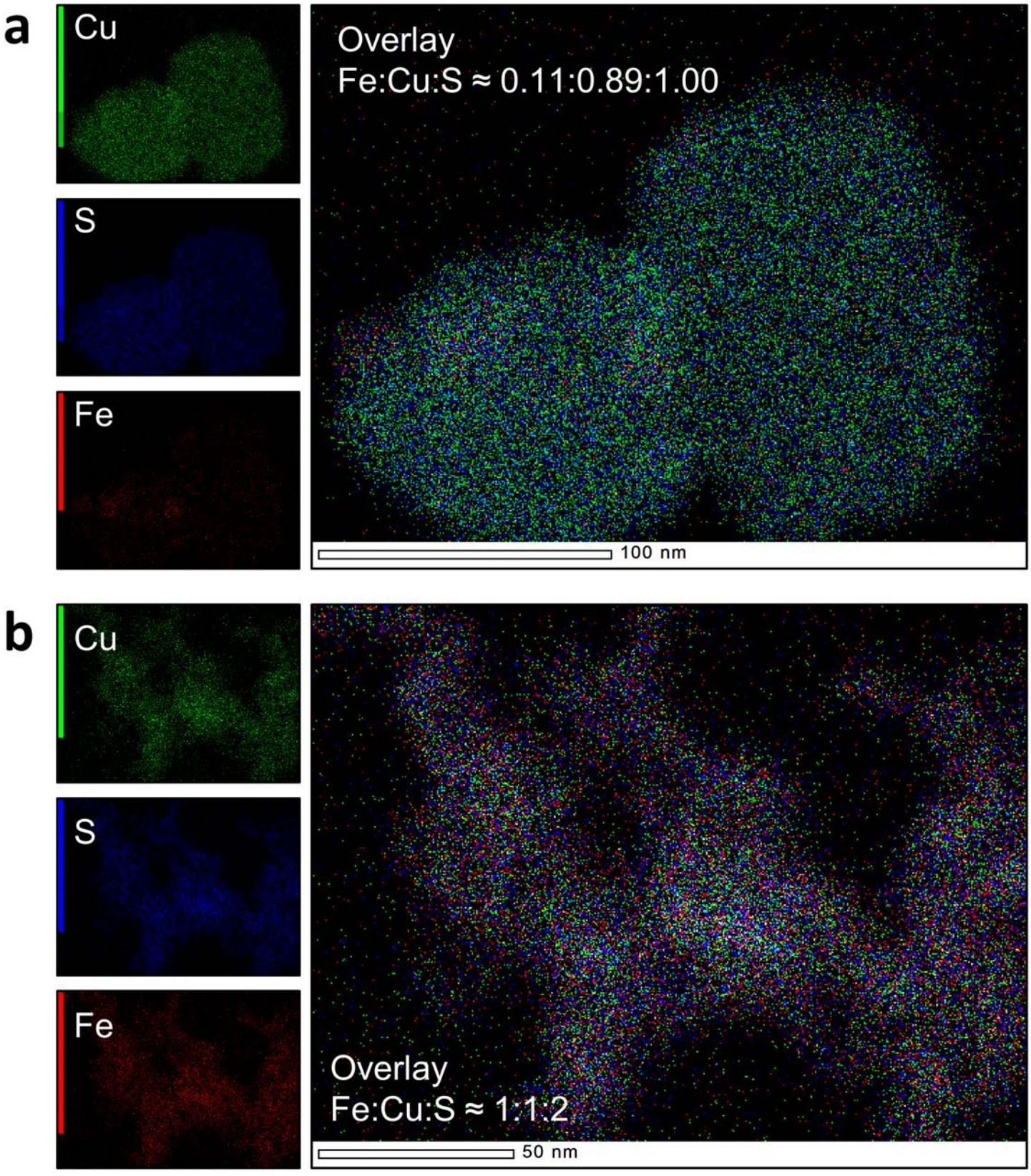

This is a preprint, the final version is subject to change, of the American Mineralogist (MSA)
Cite as Authors (Year) Title. American Mineralogist, in press.
DOI: https://doi.org/10.2138/am-2019-6848

Figure 5

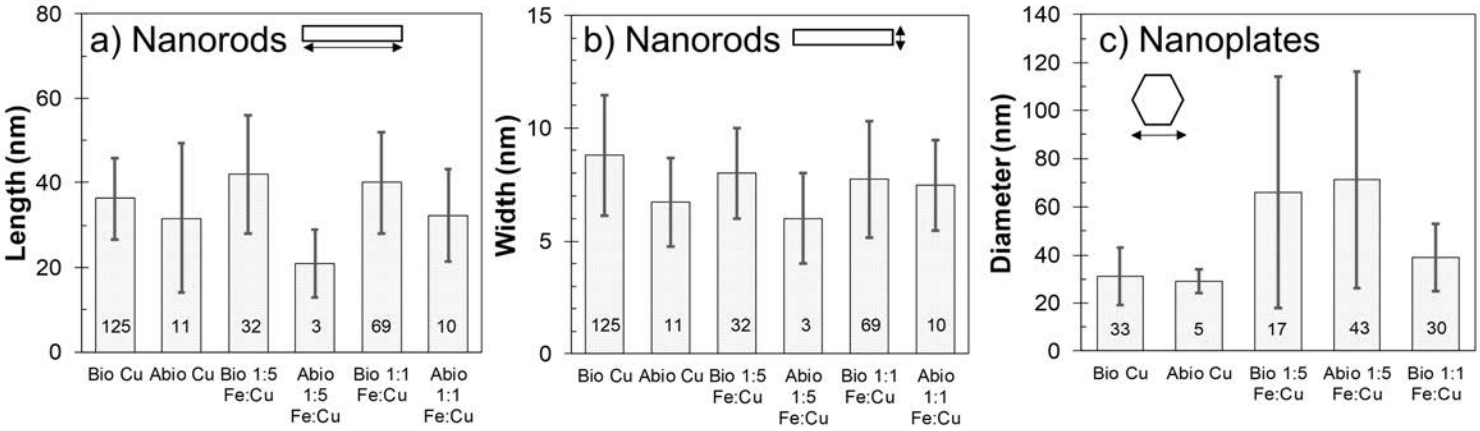

This is a preprint, the final version is subject to change, of the American Mineralogist (MSA)
Cite as Authors (Year) Title. American Mineralogist, in press.
DOI: https://doi.org/10.2138/am-2019-6848

Figure 6

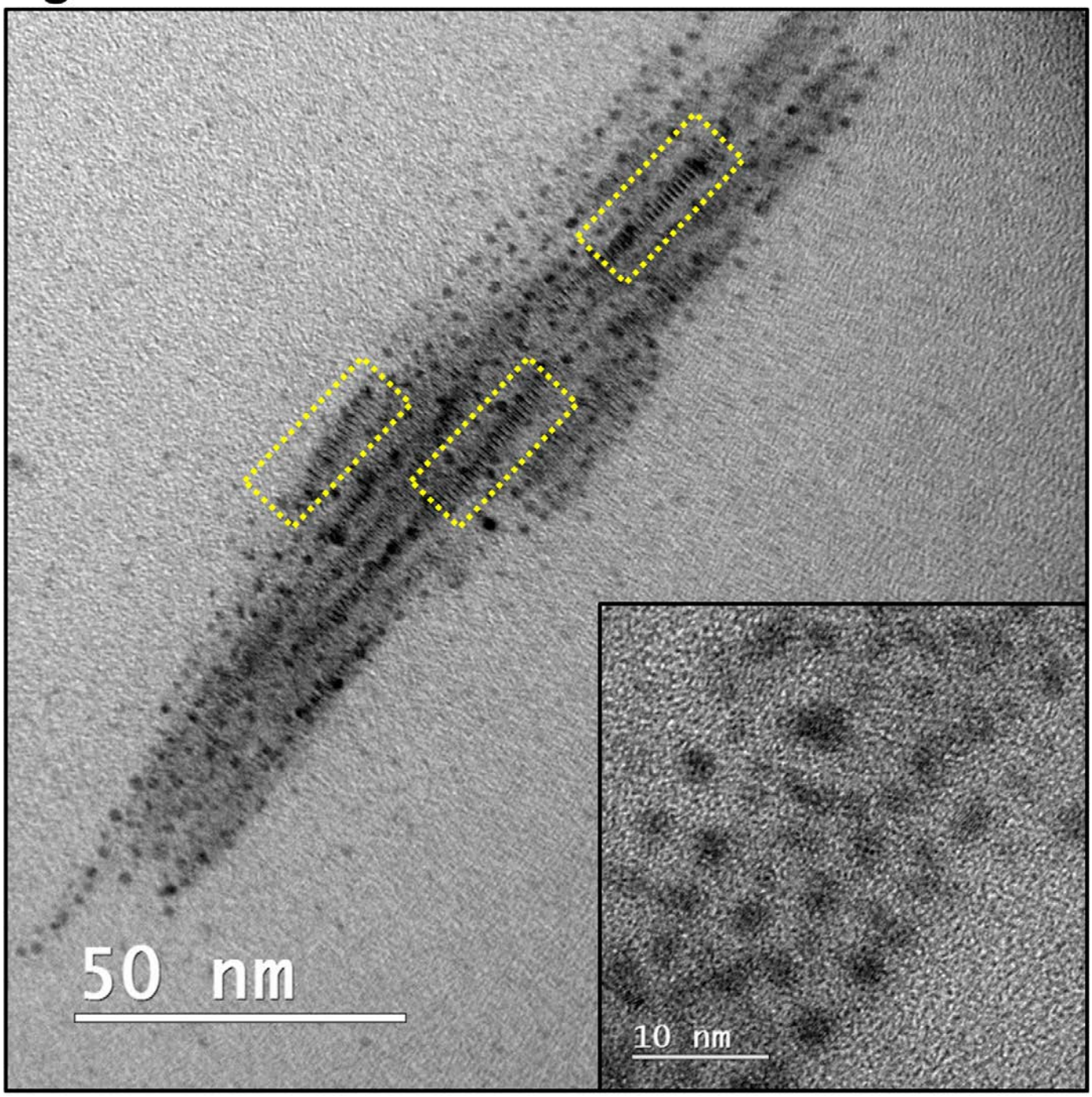

This is a preprint, the final version is subject to change, of the American Mineralogist (MSA)
Cite as Authors (Year) Title. American Mineralogist, in press.
DOI: https://doi.org/10.2138/am-2019-6848

Figure 7